Mapping responses to focal injections of bicuculline in the lateral parafacial region identifies core regions for maximal generation of active expiration

Annette Pisanski[1], Mitchell Prostebby[2], Clayton T. Dickson[1,2,3,4,5], Silvia Pagliardini[1,2,4,5*]

[1]Department of Physiology, [2]Neuroscience and Mental Health Institute, [3]Department of Psychology, [4]Department of Anesthesiology and Pain Medicine, [5]Women and Children's Health Research Institute, University of Alberta, Edmonton, AB, Canada.

*Corresponding author: Silvia Pagliardini, Department of Physiology, Faculty of Medicine & Dentistry, University of Alberta, 3020F Katz Group- Rexall Centre

Email: silviap@ualberta.ca.

Running title: Active expiration in the parafacial region

Impact statement: Multivariate analysis of the respiratory cycle shows that GABAergic disinhibition in the rostral regions of the lateral parafacial area is linked to the most significant and enduring changes in active expiration.

Authors contribution: Concept and experimental design, A.P. and S.P.; Data collection, A.P.; Data analysis, A.P. and M.P.; Manuscript preparation, A.P, M.P., C.T.D and S.P.

Keywords: active expiration; abdominal activity; bicuculline; multivariate analysis

Acknowledgements: This work was supported by CIHR Project scheme grant to SP (388717) and an NSERC Discovery operating grant to CTD (2021-02926). AP was supported by an NSERC CGS doctoral scholarship (CGSD3 – 535109 – 2019).

Abstract

The lateral parafacial area (pFL) is a crucial region involved in respiratory control, particularly in generating active expiration through an expiratory oscillatory network. Active expiration involves rhythmic abdominal (ABD) muscle contractions during late-expiration, increasing ventilation during elevated respiratory demands. The precise anatomical location of the expiratory oscillator within the ventral medulla's rostro-caudal axis is debated. While some studies point to the caudal tip of the facial nucleus (VIIc) as the oscillator's core, others suggest more rostral areas. Our study employed bicuculline (a GABA-A receptor antagonist) injections at various pFL sites (-0.2 to +0.8mm from VIIc) to investigate the impact of GABAergic disinhibition on respiration. These injections consistently elicited ABD recruitment, but the response strength varied along the rostro-caudal zone. Remarkably, the most robust and enduring changes in tidal volume, minute ventilation and combined respiratory responses occurred at more rostral pFL locations (+0.6/+0.8 mm from VIIc). Multivariate analysis of the respiratory cycle further differentiated between locations, revealing the core site for active expiration generation. Our study advances our understanding of neural mechanisms governing active expiration and emphasizes the significance of investigating the rostral pFL region.

Introduction:

The neural control of respiration is a complex physiological process that requires precise coordination among multiple brainstem nuclei. One such nucleus, the preBötzinger Complex (preBötC), plays a crucial role in generating the inspiratory rhythm and pattern (Gray, Janczewski, Mellen, McCrimmon, & Feldman, 2001; Smith, Ellenberger, Ballanyi, Richter, & Feldman, 1991; Tan et al., 2008; Wang et al., 2014). In contrast, the lateral parafacial region (pFL), also referred to as pFRG in the initial studies, has emerged as an important neuronal structure containing neurons that are responsible for the generation of active expiration via the recruitment of expiratory musculature, such as the ABD muscles (de Britto & Moraes, 2017; Huckstepp, Cardoza, Henderson, & Feldman, 2015; Pagliardini et al., 2011; Pisanski & Pagliardini, 2019). Although the involvement of preBötC in respiration, as well as its origin, anatomical markers, and anatomical location has been extensively studied (Biancardi et al., 2023; Del Negro, Funk, & Feldman, 2018; Gray et al., 2001; Hayes et al., 2017; Tan et al., 2008; Wang et al., 2014; Yackle et al., 2017; Yang & Feldman, 2018; Yang, Kim, Callaway, & Feldman, 2020), the expiratory oscillator remains a challenging structure to locate accurately due to the absence of a definite anatomical marker and the lack of its activation during experimental resting conditions (de Britto & Moraes, 2017; Magalhães et al., 2021; Pagliardini et al., 2011). Understanding the precise location and functional properties of the expiratory oscillator is crucial for unraveling the complete neural circuitry underlying respiratory control.

Previous research has employed a variety of techniques to study and elucidate this expiratory oscillator that include pharmacological disinhibition and excitation (Boutin, Alsahafi, & Pagliardini, 2017; de Britto, Magalhães, da Silva, Paton, & Moraes, 2020; de Britto & Moraes, 2017; Korsak, Sheikhbahaei, Machhada, Gourine, & Huckstepp, 2018; Magalhães et al., 2021; Pagliardini et al., 2011; Zoccal et al., 2018), as well as chemogenetic and optogenetic approaches (Huckstepp et al., 2015; Pagliardini et al., 2011; Pisanski, Ding, Koch, & Pagliardini, 2019). The coordinates used for the latter studies considered the core of the expiratory oscillator proximal to the caudal tip of the facial nucleus (VIIc) (-0.2 to +0.5 mm from VIIc). Interestingly, the use of chemogenetics

to inhibit pFL at the level of the caudal tip of the facial nucleus (-0.3 to +0.3 mm from VIIc) was unable to achieve complete inhibition of the putative expiratory muscle output, with ABD recruitment still occurring naturally during sleep, albeit at a diminished rate (Pisanski et al., 2019). Similarly, chemogenetic inhibition of pFL at +0.5 mm from VIIc significantly decreased the intensity of the ABD signals obtained in response to bicuculline/strychnine injections, but did not silence it entirely (Huckstepp et al., 2015). This evidence could suggest that the expiratory oscillator expands beyond the limits of the viral expression achieved in said studies. Intriguingly, other studies (Silva, Oliveira, Souza, Moreira, & Takakura, 2019) located its core at more rostral coordinates (+0.3 to +1.0 mm from VIIc). This dichotomy in the coordinates used to study the functional properties of the expiratory oscillator demonstrates that the characterization of the anatomical and functional boundaries of pFL are incomplete.

To address this gap, we used focal injections along different rostrocaudal locations of the brainstem to create a functional map of the pFL. Bicuculline, a competitive antagonist of γ-aminobutyric acid type A (GABA-A) receptors, has been widely employed to study neuronal excitability and functional circuitry in various brain regions, including the pFL (Pagliardini et al., 2011). By strategically administering localized volumes of bicuculline at multiple rostrocaudal levels of the ventral brainstem, we aimed to selectively enhance the excitability of neurons driving active expiration, thereby revealing the precise location and functional boundaries of the expiratory oscillation within the pFL. Using a novel multidimensional cycle-by-cycle analysis specifically developed for this study, we characterized the effect that bicuculline elicited on the different phases of the respiratory cycle at each injection site, as the differences in area under the curve of the airflow, ∫DIA EMG and ∫ABD EMG, as well as the combined differences of these three respiratory signals using a novel phase-plane analysis. This approach enabled us to construct a comprehensive functional map of the pFL in conjunction with anatomical immunostaining techniques.

Our results indicate that the injection of bicuculline produced active expiration at all locations studied (-0.2 mm to +0.8 mm from VIIc). However, the strongest effects in terms of changes in tidal volume (V_T), minute ventilation (V_E) and differences in

combined respiratory signals were observed at the two most rostral locations (+0.6 mm and +0.8 mm). Similarly, ABD activation lasted longer at these sites and the swiftest onset of the ABD response was observed at the +0.6 mm location. Interestingly, our multivariate analysis of the respiratory cycle permitted further differentiation of the response elicited in the two rostral locations, with the strongest deformations of the respiratory loop during late-Expiration (late-E) and post-Inspiration (post-I) with injections at the +0.8 mm locations, whereas injections at the level of +0.6 mm producing more pronounced deformations of the respiratory cycle during the inspiratory phase. The use of the multi dimensional trajectory map will certainly enhance our understanding of the role that the expiratory oscillator plays in respiratory control. Additionally, it will provide a crucial foundation for future investigations into its modulation, plasticity, and potential therapeutic targets for respiratory disorders.

Methods

Experimental Subjects

Thirty-five adult male Sprague Dawley rats weighing 340.4 g ± 13.2 were used for the study. The rats were housed in a controlled environment with a 12-hour light-dark cycle and were allowed unrestricted access to food and water. All experimental procedures followed the guidelines set by the Canadian Council of Animal Care and received approval from the Animal Care and Use Committee (ACUC) of the University of Alberta (AUP#461).

Surgical Preparation

Prior to the experiment, the rats were initially anesthetized using 5% isoflurane in air for induction, followed by 1-3% isoflurane for maintaining a surgical plane of anesthesia. During this time, we cannulated the femoral vein to facilitate the gradual administration of urethane (1.5-1.7 g/kg body weight) for inducing permanent and irreversible anesthesia. We assessed the depth of anesthesia by monitoring the absence of the withdrawal reflex. We cannulated the trachea and used a flow head connected to a transducer (GM Instruments, UK) to detect respiratory flow. We provided supplemental oxygen (30%) throughout the experiment and connected a gas analyzer to the tracheal tube to measure oxygen consumption. Paired electromyogram (EMG) wire electrodes (Cooner Wire, CA, USA) were inserted into the oblique ABD and diaphragm (DIA) muscles. The wires were connected to differential amplifiers (AM Systems, WA, USA), and we sampled the activity at a rate of 1kHz using the Powerlab 16/30 system (AD Instruments, CO, USA). We performed vagotomy by resecting a 2 mm portion of the vagus nerve at the mid-cervical level, and the rats' body temperature was maintained at a constant level of 37±1°C using a servo-controlled heating pad (Harvard Apparatus, MA, USA).

Bicuculline Injections

Following the surgical preparation, we placed the instrumented rats in a prone position on a Kopf stereotaxic frame. We trimmed and aseptically cleaned the incision area and achieved access to the brainstem by partially removing the occipital bone. We

144 determined the coordinates for injection into the ventral medulla with Bregma positioned
145 5 mm below lambda. The bicuculline/fluorobeads solution (n=28, 200 μM in HEPES,
146 Sigma-Aldrich) or saline/fluorobead (CTRL, n=7) was bilaterally pressure-injected into
147 specific coordinates using a sharp glass micropipette (30 μm tip diameter) at a rate of
148 100 nL/min (total volume injected was 200 nL per side). Each rat was injected at a
149 specific coordinate based on the following groups: -0.2 mm from the caudal tip of the
150 facial nucleus (VIIc) (n=5), +0.1 mm from VIIc (n=7), +0.4 mm from VIIc (n=5), +0.6 mm
151 from VIIc (n=6), +0.8 mm from VIIc (n=5), and CTRL (n=7). We recorded the
152 physiological responses to the injection for 20-25 min.

153 *Histology Procedures*

154 Upon completion of the experiments, we transcardially perfused the rats with saline
155 (0.9% NaCl), followed by 4% paraformaldehyde in phosphate buffer. We then collected,
156 postfixed, cryoprotected, and sectioned the brains in a cryostat (Leica, CM1950) to
157 obtain 30 μm thick transverse slices. To prepare the brain tissue for
158 immunohistochemistry, we washed the brain sections multiple times with phosphate-
159 buffered saline (PBS) to remove the cryoprotectant solution. All immunostaining
160 procedures were conducted at room temperature. We incubated the sections in a
161 blocking solution (0.3% Triton X-100 and 10% normal donkey serum (NDS) in PBS) for
162 1 hour to enhance membrane permeability to antibodies and minimize nonspecific
163 binding. After blocking, we incubated the tissue overnight with the primary antibody
164 solution, which consisted of PBS, 1% NDS, and 0.3% Triton X-100. In order to identify
165 specific brain structures relevant to this study, we used the following primary antibodies:
166 anti-choline acetyltransferase (ChAT; goat; 1:800; EMD Millipore, ON, Canada), anti-
167 phox2b (phox2b; mouse; 1:100; Santa Cruz Biotechnology, TX, US), anti-cFos (cFos,
168 rabbit, Cell Signaling Technology, MA, US), and anti-tyrosine hydroxylase (TH, chicken,
169 EMD Millipore, ON, Canada). The next day, we washed the tissue three times in PBS
170 and incubated it for 2 hours in a secondary antibody solution containing PBS, 1% NDS,
171 and specific secondary antibodies (1:200; Cy3-donkey anti-goat; Cy5-donkey anti-
172 mouse; Cy2-donkey anti-rabbit; rhodamine-red-donkey anti-chicken; Jackson
173 ImmunoResearch Laboratories, PA, US). Following the incubation with the secondary

174 antibodies, we washed the sections three times and mounted them with Fluorsave
175 mounting medium (EMD Millipore, ON, Canada). We observed the slides under an Evos
176 FL fluorescent microscope (Thermofisher Scientific, MA, US) and acquired TIFF files for
177 cell counting and analysis of the rostrocaudal, mediolateral, and dorsoventral
178 coordinates of the injection sites using ImageJ. We examined serial sections with a 120
179 μm interval, spanning from 400 μm caudal to 1000 μm rostral to the caudal tip of the
180 facial nucleus (VIIc). To group the animals according to the location of the injections, we
181 calculated a 3D distance from the VIIc using the rostrocaudal, mediolateral, and
182 dorsoventral coordinates of each injection site.

183 *Data Acquisition and Analysis*

184 EMG signals were amplified at ×10,000 and filtered between 300 Hz and 1 kHz (model
185 1700, AM-systems, CA, USA). The data was sampled at a rate of 1 kHz (using an
186 automatic anti-aliasing filter at 500Hz) using the PowerLab 16/35 acquisition system
187 and analyzed using LabChart7 Pro (ADInstruments), Excel 2013, Origin 9 (OriginLab
188 Corp., Northampton, MA, USA), as well as custom scripts written in MATLAB (The
189 Mathworks Inc.). All raw EMG data were digitally rectified and integrated using a time-
190 constant decay of 0.08s. Respiratory airflow was further used to determine respiratory
191 rate, V_T, and Ve. The tidal volume was obtained by integrating the airflow amplitude and
192 converting it to milliliters using a five-point calibration curve (0.5–5 ml range).

193 Airflow and integrated EMG signals were standardized across rats by first zeroing
194 signals in the rest period phases between breaths as recorded during baseline
195 conditions and then converting the remaining amplitude values into standard deviation
196 units (SD) based on a time-collapsed amplitude distribution. Data was tracked in time
197 bins of 2-minute duration from the baseline period prior to injections and spanned 20
198 min of recording post-injection. Mean-cycle measurements for each signal were
199 computed by averaging across all cycles within a given time bin. To assess the changes
200 within each of the phases of the breathing cycle, each mean-cycle was subdivided into
201 the Late-E, inspiratory, Post-I, and resting phases using the zero-crossings of the mean
202 airflow signal (Green lines, Figure 1B). The inspiratory phase begins with an inward
203 (positive going) intake of air as airflow increases above zero and ends when airflow

204 crosses zero towards the negative direction. This negative going deflection begins the
205 Post-I phase, which lasts until airflow returns to zero during the rest period. The Late-E
206 phase is defined in two ways. In cases where a significant negative deflection in airflow
207 was observed previous to inspiration, the late-E phase was determined to have begun
208 when airflow decreased below zero and ended when airflow crossed back above zero to
209 begin the subsequent inspiratory phase. When airflow did not decrease below zero prior
210 to inspiration, as was often the case during baseline conditions, the late-E phase was
211 determined as the last quarter of the expiratory period (Figure 1B). The Area under the
212 curve (AUC) was measured during baseline and was subtracted from the corresponding
213 AUC of the response for each time bin (Figure 1C). Note that areas calculated below
214 the zero- (0) line, as would be expected from a negative airflow during expiration, yields
215 negative AUC values. Any changes to the duration of the three respiratory phases, as
216 well as changes to the entire respiratory period were independently assessed using the
217 triggers described above.

218 We further contrasted the overall changes to the three respiratory signals elicited across
219 injection locations by combining them into a multi-dimensional (3D) space (Figure 1D).
220 In a manner similar to respiratory pressure-volume loops, each point in time is defined
221 as a dot in this 3D space based on the 3 simultaneous physiological measurements of
222 respiration we recorded (airflow, together with the ∫DIA EMG, and ∫ABD EMG). Each
223 respiratory cycle could then be plotted as a trajectory of points in this space,
224 represented as a loop. Example loops for the baseline and the first 2-minute time bin of
225 the elicited response are shown in Figure 1D and are also projected onto separate 2D
226 planes in Figure 1E. Our approach was to measure how the trajectories of response
227 loops changed relative to the baseline loop during each phase of the respiratory cycle,
228 as per the color scheme (same as in Figure 1B). Given these loops may be deformed
229 as a result of changes to any one of the three signals which form the basis of this 3D
230 space, this method determines the *total* extent to which breathing is altered in response
231 to stimulation. We quantified changes to respiratory trajectories elicited by bicuculline
232 injection using the sum of the “straight-line” or “Euclidean” distances between points on
233 the response and baseline loops in each respiratory phase. An example of the
234 Euclidean distance between the peak of inspiration in baseline and response loops is

shown in Figure 1F (pink line). To compute this distance for all time points, we resampled the response to ensure that that baseline and response mean-cycles had the same number of comparison phase points in a given respiratory phase. Distances were then calculated between these baseline and response loops at each timepoint *t* using the Euclidean distance formula:

$$Euclidean\ Distance_t = \sqrt{AirDiff_t^{\ 2} + DiaDiff_t^{\ 2} + AbdDiff_t^{\ 2}}$$

where $AirDiff_t$, $DiaDiff_t$ and $AbdDiff_t$ are the differences between the response and baseline mean-cycles at timepoint *t*. Averaging the distances measured at every timepoint in a given respiratory phase yields the mean Euclidean distance measure used in the analyses displayed in Figure 6G.

We extended our multivariate analysis of respiration to account for the cycle-by-cycle variability in the recorded signals. At each timepoint, we compared how far away the response mean-cycle is from the baseline mean-cycle relative to the covariance across all baseline cycles. Thus, this measure can be interpreted as having units of standard deviation, as it describes how likely it is to observe the response given the distribution of baseline measurements gathered across many respiratory cycles. This measure is known as the Mahalanobis distance and is exemplified as the pink distance relative to the black cloud of points in the baseline mean-cycle of Figure 1F. Similarly to above, this distance is computed for each timepoint *t*:

$$Mahalanobis\ Distance_t = \sqrt{(R_t - \mu_t)\sum_t^{-1}(R_t - \mu)'}$$

where R_t is the response mean-cycle at timepoint *t*, μ_t is the baseline mean-cycle at timepoint *t*, and $\sum_t$ is the covariance of all baseline cycles at timepoint *t*. Similar to the Euclidean distance above, we the calculated Mahalanobis distances across all timepoints with each respiratory phase and then averaged them across cycles to assess the mean Mahalanobis distance.

Statistics

We tested the assumptions of homogeneity of variance and normal distribution using the Brown–Forsythe ($\alpha = 0.05$) and Shapiro–Wilk ($\alpha = 0.05$) tests, respectively. Comparisons between injection locations were carried out across time bins using a two-way repeated-measures analysis of variance (two-way RM ANOVA; one repeated factor; $\alpha = 0.05$) where appropriate. In case of significant main effects, we conducted pairwise multiple comparisons post-hoc procedures (Bonferroni method; $\alpha = 0.05$). Analysis of the peak response across injection locations and in comparison to baseline, was done using a repeated measures analysis of variance (one-way repeated measures ANOVA; $\alpha = 0.05$). Upon finding significant main effects, we used Bonferroni post hoc test ($\alpha = 0.05$). In cases where assumptions of normality were rejected ($p < 0.05$), we compared responses across injection location via a Kruskal-Wallis test and following with a post-hoc Dunn test, adjusting the alpha value for multiple comparisons with Sidak's method.

Results

Histological Analysis

For each rat, we precisely identified the core of the injection sites by assessing the rostrocaudal coordinates obtained from sections containing fluorobeads. Based on the core coordinates, experiments were divided into 5 groups in which injection spanned from -0.2 mm caudal to the tip of the facial nucleus (VIIc) to +0.8 mm rostral to VIIc (as illustrated in Fig 2 B). It is noteworthy that all injections were consistently positioned ventrolateral to the facial nucleus, and there was no overlap observed between the fluorobead-marked injection sites and PHOX2B+ cells within the more ventro-medial retrotrapezoid nucleus (RTN), as depicted in Figure 2 A-B. Additionally, the injection sites were confirmed not to overlap with the soma of TH+ cells in either the caudal C1 or the more rostral A5 areas, as shown in Figure 2 A-B.

To assess the cellular responses surrounding the injection sites, we quantified both cFos+ and cFos+/PHOX2B+ cells within a defined region surrounding the fluorobead-marked areas in the pFL (as outlined in Figure 2 A). In rats injected with HEPES buffer (control group), we observed an average activation of 44.7 ± 4.0 cells per hemisection along the rostrocaudal axis of the ventral medulla (n=7). Among these activated cells, an average of 2.3 ± 1.0 cells per hemisection were also positive for PHOX2B, as illustrated in the inset of Figure 2 C. In contrast, rats injected with bicuculline displayed a distinct response pattern, characterized by a peak activation with an average of 104.5 ± 5.1 cFos+ cells localized at the core of each injection site (-0.2 mm = 89.7; +0.1mm = 123.1; +0.4mm = 110.2; +0.6mm = 98.3; +0.8mm = 101.2) (Figure 2C). Importantly, the number of cFos+ cells decreased to 44.8 ± 1.2 per section beyond the boundaries of the injection area for each experimental group. On the other hand, the number of cFos+/PHOX2B+ cells remained consistent between the control (CTRL) animals (2.3 ± 1.0 cFos+/PHOX2B+ cells per hemisection) and those injected with bicuculline (2.4 ± 0.4 cFos+/PHOX2B+ cells). These findings strongly suggest that bicuculline specifically activated cells within the vicinity of the injection sites and did not spread and activate PHOX2B+ cells in the RTN area, beyond their baseline level of activity.

Characteristics of ABD signals across the rostrocaudal axis of pFL

We successfully elicited ABD responses with the administration of bicuculline at all tested injection sites. The ABD response was most reliably triggered at locations rostral to the tip of VIIc. This observation is supported by the fact that the caudal location (-0.2 mm from VIIc) elicited responses in only 3 out of 5 rats, whereas all other groups consistently induced responses in all rats (n=5-7 rats /group). The elicited response was characterized by a late-E component in the ∫ABD EMG trace across all experimental groups (Figure 2D), as well as a downward deflection in airflow, signifying forced exhalation of the respiratory reserve volume preceding inspiration (i.e., active expiration; Figure 2D). Remarkably, in the most rostral groups (+0.6 and +0.8 mm rostral to VIIc), the ∫ABD EMG traces exhibited a tonic expiratory component, which preceded the late-E peak and was absent in the most caudal locations (-0.2 mm, +0.1 mm, and +0.4 mm). Additionally, 5 out of 6 rats in the group with injection sites at +0.6 mm rostral to VIIc, exhibited a post-I ABD peak, a feature that was absent in all other groups (Figure 2D).

Temporal dynamics of the ABD response reveal a longer-lasting and fastest response at rostral locations

The temporal characteristics of the ∫ABD EMG signal elicited by bicuculline injections at different rostrocaudal locations exhibited notable variations. Overall, responses had a shorter duration in the most caudal locations (-0.2 mm; +0.1 mm; + 0.4 mm) compared to the rostral locations (+0.6 mm; +0.8 mm) (Figure 3A). In all groups, the ABD response initiated following the second bicuculline injection, except at location +0.6 mm, where it commenced following the first injection and became more pronounced with the second injection (Figure 3 A). Across all groups, the most robust ABD responses, as measured by ∫ABD EMG amplitude, were observed within the first 2 min of the response, declining to zero in the last 2 min (18 min post-injection) in the most caudal groups (-0.2 mm; +0.1 mm; + 0.4 mm). In contrast, these responses remained present, albeit weaker, in the most rostral groups (+0.6 mm; +0.8 mm) after 20 min from injection (Figure 3 B-C).

The coupling of the ∫ABD EMG and ∫DIA EMG signals, which reflects the robustness of the response and the coupling between inspiratory and expiratory oscillators, was notably weaker at the most caudal location (-0.2 mm = 0.6 ± 0.2) in comparison to the

most rostral groups (+0.4 mm = 0.96 ± 0.02; +0.6 mm = 0.89 ± 0.05; +0.8 mm = 0.97 ± 0.02) (One-Way ANOVA p = 0.015; Tukey -0.2 mm vs +0.4 mm: p = 0.024; -0.2 mm vs +0.6 mm: p = 0.048; -0.2 mm vs +0.8 mm: p = 0.029) (Figure 3 D). Similarly, the ABD response duration was significantly longer at the two most rostral locations (+0.6 mm = 17.6 ± 2.7 min; +0.8 = 17.1 ± 3.3 min) compared to the most caudal group (-0.2 mm = 2.4 ± 1.1 min) (One-Way ANOVA p = 0.043; Tukey -0.2 mm vs +0.6 mm: p = 0.048; -0.2 mm vs +0.8 mm: p = 0.041) (Figure 3E). Lastly, the group with injection sites located at +0.6 mm initiated responses significantly sooner than all other groups (-0.2 mm = 20.3 ± 13.4 sec; +0.1 mm = 32.5 ± 20.6 sec; +0.4 = 40.1 ± 28.7 sec; +0.8 = 23.1 ± 19.8 sec), with an average response delay of 88.7 ± 32.3 sec previous to the second injection (but after the first one), which is represented as negative values (One-Way ANOVA p= 0.041; Tukey -0.2 mm vs +0.6 mm: p = 0.039; +0.1 mm vs +0.6 mm: p = 0.040; +0.4 mm vs +0.6 mm: p = 0.045; +0.8 mm vs +0.6 mm: p = 0.049) (Figure 3 F). In summary, these results underscore that injections at the most rostral locations (+0.6 mm and +0.8 mm) elicit more robust and prolonged ABD responses than the caudal location (-0.2 mm). Furthermore, bicuculline injections at +0.6 mm from VIIc initiated the fastest response, suggesting proximity to the cells responsible for ABD recruitment following bicuculline injection.

Bicuculline injection elicited stronger respiratory effects at the rostral locations

The ABD response elicited by bicuculline injection generated a late-E downward inflection in airflow that was absent in baseline conditions (Figure 4 A). We measured the late-E peak amplitude and area to assess the strength of the response across different rostrocaudal locations. On average, the late-E peak amplitude and area values reached a maximum between 2- and 4-min post-second injection for all rostrocaudal locations except the most rostral injection site (+0.8 mm from the tip of VIIc), which peaked between 6- and 8-min post-second injection (Figure 4 B,D). Although the late-E peak amplitude seemed to reach a higher maximum in the two most rostral groups (+0.6 mm = -0.033 ± 0.007 V; +0.8 mm = -0.027 ± 0.011 V), these values were not significantly different when compared to the remaining locations (-0.2 mm= -0.014 ± 0.004 V; +0.1 mm = -0.021 ± 0.007 V; +0.4 mm = -0.023 ± 0.004 V) (One-Way ANOVA

p= 0.41) (Figure 4 C). Similarly, the late-E peak area also seemed to reach a higher maximum in the two most rostral locations (+0.6 mm = -0.0056 ± 0.0010 V.s; +0.8 mm = -0.0047 ± 0.0019 V.s), but these values were not significantly different from the rest of the injection sites (-0.2 mm= -0.0014 ± 0.0007 V.s; +0.1 mm = -0.0035 ± 0.0015 V.s; +0.4 mm = -0.0038 ± 0.0011 V.s) (One-Way ANOVA p= 0.30) (Figure 4 E).

The injection of bicuculline along the rostrocaudal axis of the ventral medulla induced a drop in respiratory frequency in all the injection sites tested (Figure 4 F), but this drop in frequency was only significant in comparison to baseline in the two most caudal groups (One-Way repeated measures ANOVA p = 0.003; Bonferroni: -0.02 mm baseline vs injection, p = 0.03; +0.1 mm baseline vs injection, p = 0.005) (Figure 4 G). The respiratory rate reached a minimum value of 37.08 ± 1.36 bpm (12% drop from baseline) at 2 min post-injection in the most caudal location (-0.2 mm), whereas the minimum respiratory frequency value was reached at 4 min for the middle groups (+0.1 mm = 37.2 ± 2.0 bpm – 17% drop from baseline; +0.4 mm = 40.1 ± 1.6 bpm – 9% drop from baseline) and 6 min for the most rostral injection sites (+0.6 mm = 38.6 ± 2.6 bpm – 10% drop from baseline; +0.8 mm = 39.1 ± 2.2 bpm – 11% drop from baseline) (Figure 4 F). Interestingly, the duration of inspiration during the response was found to significantly decrease in all groups relative to baseline respiration (T_i response = 0.279 ± 0.034s, T_i baseline = 0.318 ± 0.043s, Wilcoxon rank sum: Z = 3.24, p = 0.001). Inspiratory time also decreased following bicuculline injections relative to control injections (T_i control = 0.326 ± 0.024s) and remained lowered throughout the response, but this reduction did not attained the level of statistical significance for comparisons at the peak of the response (KW test: H(5) = 9.41, p = 0.094). Contrary to this decrease in inspiratory duration, the total expiratory time was observed to significantly increase in all groups and remained elevated compared to baseline (T_E response = 1.313 ± 0.188s, T_E baseline = 1.029 ± 0.161s, Wilcoxon rank sum: Z = 4.49, p = 0.001). As in the case of inspiratory time, the increased expiratory time did not reach statistical significance when comparing the peak responses of any of the groups including control (T_E control = 1.061 ± 0.161s, KW test: H(5) = 9.42, p = 0.094). Overall, these results suggest that the most caudal locations (-0.2 mm and +0.1 mm) experienced a faster and more drastic drop in respiratory frequency following bicuculline injection, and this reduction in frequency was

394 driven by an increase in expiratory period accompanied by a reduction in the inspiratory
395 time.

396 The amount of inspired air per each breath, measured as $V_{T,}$ significantly increased
397 when compared to baseline in all the injection sites tested except the most caudal
398 location (-0.2 mm from VIIc) (One-Way repeated Measures ANOVA, p = 0.01) (Figure 4
399 H-I). In all the groups, the increase in V_T peaked at 4 min post-injection (Figure 4 H). Of
400 particular interest is that the peak V_T observed in the +0.6 mm location (V_T = 10.8 ± 0.5
401 ml/kg – 29% increase from baseline) was significantly higher than that observed in the
402 two most caudal groups (-0.2 mm = 7.0 ± 0.4 ml/kg – 8% increase from baseline and
403 +0.1 mm = 8.0 ± 0.3 ml/kg – 16% increase from baseline) (One-Way ANOVA p = 0.01;
404 Bonferroni p = 0.03) (Figure 4 I). On the other hand, V_E decreased compared to
405 baseline in the most caudal group (-0.2 mm = 255.4 ± 16.2 ml x min^{-1} x kg^{-1} – 12% drop
406 from baseline, One-Way Repeated Measures ANOVA, p= 0.001), whereas at the +0.6
407 mm location, V_E increased following bicuculline injection (V_E = 414.3 ± 22.7 – 16%
408 increase from baseline, One-Way Repeated Measures ANOVA, p = 0.001) (Figure 4 J-
409 K). Interestingly, the change produced in V_E after injection of bicuculline at the most
410 rostral locations (+0.4 mm; +0.6 mm and +0.8 mm) was significantly larger than that
411 produced after injection at -0.2 mm from VIIc (One-Way ANOVA p = 0.0006, Bonferroni
412 p = 0.0004) (Figure 4 K). These results suggest that the V_E was mostly driven by the
413 drop in respiratory frequency at the two most caudal locations (-0.2 mm and +0.1 mm),
414 whereas V_T drove the increase in V_E observed in the most rostral groups (+0.4 mm;
415 +0.6 mm; +0.8 mm), which resulted in a more drastic increase in V_E.

416 *Injection of bicuculline decreased oxygen consumption at the rostral locations*

417 To evaluate the metabolic effects of the respiratory changes induced by bicuculline
418 injections along the rostrocaudal axis of the ventral medulla, we measured the amount
419 of oxygen consumption in the experimental animals (V_{O2}). Overall, V_{O2} remained similar
420 to baseline at the 3 most caudal locations (-0.2 mm; +0.1 mm and +0.4 mm) (Figure 4
421 L-M) and dropped from baseline only at the most rostral sites (+0.6 mm and +0.8 mm)
422 (One-Way Repeated Measures ANOVA p = 0.0001). Similarly, the minimum V_{O2}
423 achieved at the rostral groups (+0.6 mm = 11.8 ± 0.8 ml x min^{-1} x kg^{-1} – 33% drop from

424 baseline and +0.8 mm = 12.2 ± 6.1 ml x min^{-1} x kg^{-1} – 25% drop from baseline) was
425 significantly different from the values achieved at the most caudal locations (-0.2 mm =
426 17.3 ± 3.3 ml x min^{-1} x kg^{-1} – 10% drop from baseline; +0.1 mm = 17.6 ± 1.3 ml x min^{-1} x
427 kg^{-1} – 17% drop from baseline) (One-Way Repeated Measures ANOVA p = 0.0001,
428 Bonferroni p = 0.005) (Figure 4 M). Additionally, the ratio of V_E/V_{O2} remained unchanged
429 from baseline following bicuculline injection, except at the two most rostral locations,
430 where it increased (+0.6 mm and +0.8 mm) (One-Way Repeated Measures ANOVA p =
431 0.001) (Figure 4 N-O). The maximum V_E/V_{O2} was achieved at 6-8 min post-second
432 injection at the two most rostral locations (+0.6 mm = 34.8 ± 3.0 – 73% increase from
433 BL; +0.8 mm = 38.7 ± 12.8 – 82% increase from baseline) (Figure 4 N), and these
434 values were significantly different from the values observed at the two most caudal
435 groups (-0.2 mm = 20.0 ± 6.7 – 3% increase from baseline and +0.1 mm = 18.7 ± 2.8 –
436 15% increase from BL) (One-Way ANOVA p = 0.0006, Bonferroni p = 0.003) (Figure 4
437 O). In summary, these results suggest that bicuculline injection and the resulting
438 respiratory effects led to a reduction in oxygen consumption, especially at the +0.6 mm
439 and +0.8 mm locations. Furthermore, the reduction in V_{O2} paired with the increases in
440 V_E observed at the most rostral injection sites (+0.6 mm and +0.8 mm), resulted in
441 hyperventilation, an effect which was not observed in the two most caudal groups (-0.2
442 mm and +0.1 mm).

443 *Rostral bicuculine injection induces more prominent changes to all phases of the*
444 *respiratory cycle*

445 To further differentiate the responses elicited by bicuculine injections at each location
446 along the rostrocaudal axis of the ventral medulla, we subdivided our analysis by
447 respiratory phase (late-E, inspiratory, and post-I) and measured the differences in the
448 area of respiratory signals (airflow, ∫DIA EMG and ∫ABD EMG) as per the algorithm
449 described in the methods section (Figure 5 A-C).

450 Injections at all locations induced negative deflections in the airflow signal (Figure 5D)
451 and were concomitant with potent increases to the ∫ABD EMG within the late-E phase
452 (Figure 5 D,F), whereas there was no change in ∫DIA EMG signal during this phase
453 (Figure 5 E). The observed differences tended to be more prominent in rostral locations

and tended towards significance ($p < 0.1$) when comparing the late-E responses from the +0.6mm and +0.8mm injection groups to control injections for the entire duration of the 20-minute post-injection response. The expiratory airflow reached significance ($\alpha = 0.05$) when comparing the second most rostral location (+0.6mm) relative to control injections at timepoints from 4 min (KW test: $H(5) = 14.66$, $p = 0.012$, Dunn: p , 0.001) to 12 min post-injection (KW test: $H(5) = 18.35$, $p = 0.003$, Dunn: $p < 0.001$) (Figure 5D). Moreover, airflow responses were significantly more negative following bicuculline injections in the +0.6mm group compared to the -0.2mm group, and remained significantly different at several timepoints from 8 min (KW test: $H(4) = 11.41$, $p = 0.022$, Dunn: $p < 0.001$) to the last 20 min of the post-injection period (KW test: $H(4) = 10.65$, $p = 0.031$, Dunn: $p = 0.002$) (Figure 5D). In a similar manner, increases in the ∫ABD EMG response differed significantly relative to those elicited by control injections only for the 2 most rostral injection locations (+0.6mm, +0.8mm) at timepoints from 6 min (KW test: $H(5) = 16.23$, $p = 0.006$, Dunn: +0.6mm: $p < 0.001$; +0.8mm: $p = 0.002$) to 12 min (KW test: $H(5) = 20.81$, $p <0.001$, Dunn: +0.6mm: $p < 0.001$; +0.8mm: $p < 0.001$)(Figure 5F). Correspondingly, the increases in ∫ABD EMG activity evoked by these rostral locations (+0.6mm: Purple, +0.8mm: Orange) were significant as compared to the response at the most caudal location (-0.2mm: Red) for a similar range of timepoints from 8 min (KW test: $H(4) = 14.60$, $p = 0.006$, Dunn: +0.6mm: $p < 0.001$; +0.8: $p = 0.002$) to 14 min (KW test: $H(4) = 13.93$, $p = 0.008$, Dunn: +0.6mm: $p = 0.002$; +0.8mm: $p < 0.001$) with the +0.8mm group remaining significantly elevated at 16 min (KW test: $H(4) = 13.56$, $p = 0.009$, Dunn: +0.8: $p = 0.002$)(Figure 5F). Thus, our results in the Late-E phase demonstrate that the rostral regions of the ventral medulla are the most sensitive to bicuculline-induced increases in expiratory airflow, presumably elicited via a prominent activation of ABD activity.

For the inspiratory phase, bicuculline injections evoked strong increases in the respiratory airflow and ∫DIA EMG signal, which were strongest in the rostral locations (+0.6mm, +0.8mm) and relatively weaker in more caudal locations (-0.2mm). Inspiratory airflow was significantly increased relative to control injections compared to the +0.6mm group for timepoints extending from 2 min (KW test: $H(4) = 13.25$, $p = 0.021$, Dunn: $p < 0.001$) to 12 min post-injection (KW test: $H(4) = 14.58$, $p = 0.012$, Dunn: $p =$

0.001)(Figure 5D). Unlike the effects noted above within the Late-E phase, airflow increases in this group were found to only reach significance for a shorter portion of the response from 10 min (KW test: $H(4) = 10.50$, $p = 0.033$, Dunn: $p = 0.004$) to 12 min (KW test: $H(5) = 10.93$, $p = 0.027$, Dunn: $p = 0.003$) post-injection when compared to the +0.4mm group (Figure 5D). ∫DIA EMG activity did not differ significantly when compared between injection locations or to control injections, despite the increases in mean ∫DIA EMG area in the +0.6mm and +0.8mm injection groups which peaked early in the time course of the response and are visible in Figure 5E. Contributions of the ABD muscle to the respiratory changes during inspiration (Figure 5F, inspiratory phase) were determined to be negligible as the raw ABD EMG is not active during this phase and the remaining signal in the ∫ABD EMG can be accounted for by exponential decay induced by the integration algorithm used to pre-process these signals (see methods section). These results illustrate that the increases in inspiratory airflow and ∫DIA EMG activity evoked by bicuculline injections are stronger when targeting more rostral injection locations. However, these changes are relatively weak and, on average, remain altered for a much shorter period of time relative to the effects noted above for the Late-E phase.

Negative deflections in the airflow signal during the post-I phase were observed in several responses and were most pronounced in the 2 most rostral injection groups consistent with the results above (Purple and Orange, Figure 5D). However, the area-under-the-curve measure used here to quantify changes in expiratory airflow relative to baseline did not reach the level of significance at $\alpha = 0.05$ when comparing injection locations as was described above for the other respiratory phases. Bicuculline injections into the most rostral group (+0.8mm: Orange) did, however, evoke substantial increases in ∫ABD EMG activity during the post-I phase which were significantly elevated during the 6 minute (KW test: $H(4) = 10.37$, $p = 0.035$, Dunn: $p = 0.002$) and 16 minute time bins (KW test: $H(4) = 9.52$, $p = 0.049$, Dunn: $p = 0.001$) when compared to injections into the most caudal group (-0.2mm). These effects were unlikely to be related to any changes in the DIA signal, as the DIA muscle activity is quiescent during the post-I

514 period (Figure 5A) and the ∫DIA EMG is contaminated by the pre-processing as noted
515 above for the ABD muscle during inspiration (see methods section).

516 Altogether, the area-under-the-curve analysis in Figure 5 shows that airflow is
517 substantially altered in all 3 phases of the respiratory cycle and the ABD muscle is
518 strongly activated in several groups in the late-E and post-I periods with injections of
519 bicuculline along the pFL axis. Importantly, these effects are significantly stronger when
520 targeting the rostral areas of the pFL (+0.6mm and +0.8 mm from VIIc) compared to
521 injections that target the more caudal regions.

522 *Bicuculline responses following injections along the rostrocaudal axis of the ventral*
523 *medulla can be differentiated by the deviations of their 3D trajectories at different*
524 *phases of the respiratory cycle*

525 We next sought to determine whether responses to bicuculline injections across the
526 rostrocaudal axis of the pFL could be more precisely differentiated from each other
527 when combining the responses in all three recorded signals (airflow, together with ∫DIA
528 and ∫ABD EMG) evoked within the periods of late-E, inspiration, and post-I. Our
529 approach was to represent all three signals as axes in a 3-dimensional space wherein
530 each point corresponds to an individual timepoint during our recordings. When plotting
531 the measurements across an entire respiratory cycle, this multidimensional
532 representation resembles a looped trajectory as shown in Figure 1D for cycles recorded
533 during the baseline and post-injection periods. Indeed, each phase of the cycle (late-E,
534 inspiration, and post-I) could be recognized as a particular region along the 3D
535 trajectory. Inspiration, for example, occupies the space where airflow and ∫DIA EMG are
536 positive (Figure 1D: red). In baseline conditions, the loop is largely confined to the plane
537 defined by the airflow-∫DIA axes, as the ABD muscles are not activated during resting
538 states (Figure 1E, left). Following bicuculline injections, respiratory loops became more
539 complex, involving marked perturbations occurring in this first plane, together with novel
540 deformations extending along the ∫ABD EMG axis as shown in the right-hand plane in
541 Figure 1E, described by airflow and the ∫ABD EMG. The relative amplitudes of these
542 complex deviations from the baseline cycle could then be used to characterize the
543 degree of change caused by our injections across pFL sites.

Figures 6 A through E demonstrate how the trajectories computed during the baseline (shown in black) are altered as the response evolves across each time bin spanning the full 20-minute post-injection period for all injection locations. Supplementary videos of each example recording in Figure 6, along with their cycle-by-cycle variability, further clarify their 3D shape as the trajectory is rotated about the ∫DIA EMG axis (Supplementary Materials 1-5). We noted several key deformations to baseline loops including a “bulb” of activation on the outermost edge of the loop during the peak of inspiration when airflow is at its maximum. These “bulbs” are similarly confined to the ∫DIA EMG-airflow axis as both of these signals are involved in shaping their overall prominence. Baseline loops are also perturbed during the late-E period as a result of ∫ABD EMG-airflow activation which can be seen as “tails” which extend upwards in the right-most plots of Figure 6A-E. Abdominal-airflow activation during the post-I period manifests as an upwards “foot-like” extension of the cycle in left-most portion of the Figure 6 A-E, most prominently displayed in the representative recording of Figure 6D. The example trajectories in Figure 6A-E demonstrate how the deformations in each phase can be used as features to distinguish the responses of each injection location.

Consistent with our analyses above, the late-E tails of the response loops elicited by caudal injection locations are relatively smaller compared to those observed in rostral locations (Figure 6A). Moreover, these “tails” in the -0.2mm, +0.1mm, and +0.4mm groups last for a shorter duration than the two most rostral locations as can be determined by their more bluish-yellowish color (Figure 6A-E: rightmost panel). Inspiratory bulbs appear to be more similar across groups and are most prominent in the +0.6mm group (Figure 6A-E: middle panel). Lastly, post-I “feet” are largely absent in the example responses of the three most caudal groups (-0.2mm, +0.1mm, +0.4mm) and are particularly noticeable in the +0.6mm and +0.8mm groups.

Quantifying the extent of these 3 features as the Euclidean distance between bicuculline injection and baseline in each respiratory phases is displayed in Figure 6F. Compared to control injections of HEPES buffer, bicuculline evoked pronounced Late-E “tails”, as well as inspiratory “bulbs”, and post-I “feet” in all injection groups which lasted throughout the 20 min response, with the notable exception of the most caudal group (-0.2mm)

which returned to a baseline trajectory by 8 min post-injection (Figure 6G). Consistent with the results in Figure 5, the most rostral injections at +0.6mm and +0.8mm elicited the largest Late-E deformations. The 3D approach applied here further differentiated the responses of these two groups, as the Late-E “tails” of the +0.6mm group were significantly longer than those observed in the -0.2mm group early in the response from 8 min (KW test: $H(4) = 12.22$, $p = 0.016$, Dunn: $p < 0.001$) to 12 min (KW test: $H(4) = 12.34$, $p = 0.015$, Dunn: $p = 0.002$), while those in the +0.8mm group peaked later in the response and were significantly longer than in the -0.2mm group from 12 min (KW test: $H(4) = 12.34$, $p = 0.015$, Dunn: $p = 0.001$) to 16 min (KW test: $H(4) = 10.89$, $p = 0.028$, Dunn: $p = 0.001$) (Figure 6G). These results are consistent with the observations in Figure 3F, which indicate that responses in the +0.6mm group begin earlier relative to other groups. Moreover, the +0.6mm group produced the largest deformations to the inspiratory “bulb” which were significantly greater than those in the -0.2mm group from 8 min (KW test: $H(4) = 12.59$, $p = 0.013$, Dunn: $p < 0.001$) to 14 min (KW test: $H(4) = 10.27$, $p = 0.036$, Dunn: $p = 0.001$) (Figure 6G). On the contrary, the largest post-I “feet” were observed in the +0.8mm group and were significantly greater than the -0.2mm group from 4 min (KW test: $H(4) = 10.01$, $p = 0.040$, Dunn: $p = 0.002$) to 16 min (KW test: $H(4) = 9.70$, $p = 0.046$, Dunn: $p = 0.001$), excluding at the 10 minute (KW test: $H(4) = 8.93$, $p = 0.063$) and 14 minute time bins (KW test: $H(4) = 8.10$, $p = 0.088$) (Figure 6G).

As demonstrated in the representative graphs in Figure 6A-E, the variability of the respiratory trajectories within the baseline or response periods (shown as clouds around the trajectory “loop”), differs significantly between experiments. To account for the impact of this variability on our quantification of trajectory deformations, we computed the mean Mahalanobis distance within the late-E, inspiratory, and post-I phases (see methods). Our results revealed a gradient of response intensities relative to respiratory variability, with the two most rostral groups producing the strongest deformations to breathing trajectories (Figure 6H). Similar to our results above, these groups differed in the time course and relative strength of their responses in each phase. Injections at +0.6mm produced significantly more pronounced late-E “tails” compared to caudal injection responses from 6 min (KW test: $H(4) = 11.80$, $p = 0.019$, Dunn: $p = 0.001$) for

12 min (KW test: $H(4) = 12.24$, $p = 0.016$, Dunn: $p = 0.001$)(Figure 6H). Late-E “tails” from the +0.8mm group were significantly more prominent than “tails” evoked by caudal bicuculline injections for much greater proportion of the 20minute response compared to the +0.6mm group, ranging from 6 min (KW test: $H(4) = 11.80$, $p = 0.019$, Dunn: 0.002) to 20 min post-injection (KW test: $H(4) = 11.01$, $p = 0.026$ Dunn: $p < 0.001$) (Figure 6H). Deformations to the inspiratory “bulb” relative to respiratory variability were significantly larger in the +0.6mm group compared to caudal responses and peaked at the 12minute time bin post-injection (KW test: $H(4) = 10.63$, $p = 0.031$, Dunn: $p = 0.002$)(Figure 6H). In contrast, the extent of post-I “feet” was significantly greater in the +0.8mm group than the -0.2mm group from 6 min (KW test: $H(4) = 11.00$, $p = 0.027$, Dunn: $p = 0.002$) to 20 min (KW test: $H(4) = 10.74$, $p = 0.030$, Dunn: $p < 0.001$), where as the extent of post-I “feet” in the +0.6mm group was significantly greater than in caudal injections only at the 8 minute (KW test: $H(4) = 11.65$, $p = 0.020$, Dunn: $p = 0.002$) and 12 minute time bins (KW test: $H(4) = 12.23$, $p = 0.016$, Dunn: $p = 0.001$). Thus, while response intensity in all respiratory periods was strongest in the two most rostral injection groups, overall changes in the late-E and post-I period were strongest in the +0.8mm group, while changes in inspiration were strongest in the +0.6mm group.

Discussion

In this study, our primary aim was to investigate the rostro-caudal distribution of the source of active expiration within the lateral parafacial region (pFL). To accomplish this objective, we used bicuculline, a GABA-A receptor antagonist known for its ability to disinhibit pFL cells (de Britto & Moraes, 2017; Huckstepp et al., 2015; Pagliardini et al., 2011; Silva et al., 2019). Bicuculline was administered at various rostro-caudal coordinates, and we methodically assessed the resulting respiratory responses to pinpoint the location within this region that induced the most significant and relevant changes to the respiratory cycle. Our findings offer valuable insights into the neural circuitry governing active expiration in the brainstem, with a particular focus on less-explored, more rostral areas of the pFL.

Histological Analysis

We adopted a stereological approach to identify the central region of the injection sites by visualizing sections containing fluorobeads. Experimental subjects were categorized based on the proximity of the injection sites, spanning from -0.2 mm to +0.8 mm from VIIc. We took measures to ensure that injections were positioned ventrolateral to the facial nucleus (VIIc) and did not overlap with PHOX2B+ cells within the more ventromedial retrotrapezoid nucleus (RTN). Evaluation of cellular activity following bicuculline activation, as measured by cFos staining, confirmed minimal baseline activity of the PHOX2B+ cells in all groups as compared to the control group. These results confirm very limited mediolateral spread of the drug from the core site of injection and support previous findings indicating that PHOX2B is not a marker for the expiratory oscillator (de Britto & Moraes, 2017; Magalhães et al., 2021).

Characteristics of ABD Signals

Our efforts successfully elicited expiratory ABD responses and active expiration at all tested injection sites, consistent with previous reports (Boutin et al., 2017; de Britto et al., 2020; de Britto & Moraes, 2017; Huckstepp et al., 2015; Korsak et al., 2018; Magalhães et al., 2021; Pagliardini et al., 2011; Silva et al., 2019; Zoccal et al., 2018). Previous work has primarily examined the core of pFL at locations ranging from -0.2 mm

651 to +1.0 mm from the caudal tip of the facial nucleus, a range similar to the one explored
652 in the current study (-0.2 mm to +0.8 mm from VIIc). However, it is important to note that
653 those studies have traditionally used the presence or absence of active expiration in
654 response to a stimulus as the only measure to determine the location of pFL. Our study
655 reveals that this metric is not the most accurate in determining the closest proximity to
656 the pFL core, as we found that all locations within that range in which injections were
657 made exhibited active expiration. Consequently, we employed a combination of diverse
658 respiratory measures to assess the injection site that induced the most robust
659 respiratory effect.

660 Remarkably, the ABD response was consistently generated at locations rostral to VIIc,
661 aligning with previous observations that did not find a reliable triggering of the ABD
662 response at caudal positions ranging from -0.2 mm to -0.4 mm from VIIc (Pagliardini et
663 al., 2011). This response was characterized by a late-E component at all rostro-caudal
664 locations and, in the most rostral groups (+0.6 mm and +0.8 mm from VIIc), an
665 additional tonic post-I component that was absent in the injections at more caudal
666 locations. Although the configuration of the ABD response, whether late-E only, tonic, or
667 a combination of the two, has not been extensively discussed in the literature, these
668 distinctions may provide valuable insights into the involvement of distinct neuronal
669 circuits in mediating the ABD response. For example, sample traces from the injection
670 of bicuculline/strychnine from 0 to +1.0 mm from VIIc with 4-5% CO_2 exposure exhibited
671 a tonic ABD response throughout the entire expiratory phase (without post-I or late-E
672 peaks) (Silva et al., 2019), whereas sample traces from injections spanning from -0.2
673 mm to +0.4 mm from VIIc seemed to indicate a combination of tonic and late-expiratory
674 ABD responses (de Britto & Moraes, 2017; Pagliardini et al., 2011). Interestingly, the
675 latter studies also observed tonic increases in ABD EMG (without a late-expiratory
676 peak), but only during baseline conditions and not in response to drug injection. In our
677 study, we also observed a post-I ABD activation that only appeared at the +0.6 mm
678 location. This post-I peak was previously observed in neonate rats (postnatal day 5)
679 during ABD activation occurring throughout apneic periods induced by systemic fentanyl
680 injection (Janczewski, Onimaru, Homma, & Feldman, 2002). A similar biphasic pattern
681 (late-E/post-I) was also observed in facial nerve recordings of *in vitro* preparations and

682 associated with neuron activity in the parafacial area (Onimaru & Homma, 2003;
683 Onimaru, Kumagawa, & Homma, 2006). The presence of these unique response
684 features at different rostro-caudal locations suggests a complex interplay among neural
685 populations within the ventral medulla, necessitating further investigation beyond the
686 scope of the present study.

687 *Temporal dynamics of the ABD response reveal a longer-lasting and shortest latency*
688 *response at rostral locations*

689 The temporal dynamics of the ABD response exhibited significant variations along the
690 rostro-caudal axis. Responses at rostral locations displayed prolonged durations and
691 stronger coupling with DIA signals compared to caudal locations. Previous research
692 employing bicuculline injections to induce active expiration have reported an increase in
693 the coupling of ABD/DIA signals +0.1mm to +0.3 mm from VIIc in juvenile rats (de Britto
694 & Moraes, 2017). Similarly, we observed good ABD/DIA coupling at locations rostral to
695 +0.1 mm. Such coupling has been documented in other studies as an indicator of the
696 robustness of the ABD response, either during hypercapnia/sleep or chemogenetic
697 modulation during sleep (Leirão, Silva, Gargaglioni, & da Silva, 2018; Pisanski et al.,
698 2019). Therefore, in our study, we used it as a measure of the strength of the achieved
699 ABD activation. Additionally, prior studies have indicated that the duration of effects
700 induced by bicuculine/strychnine injections at locations spanning from -0.2 mm to +1.0
701 mm from VIIc can range from 16 to 30 min (Pagliardini et al., 2011; Silva et al., 2019).
702 However, these studies did not specify whether there were disparities in the duration of
703 ABD responses along the rostro-caudal axis. In our study, we have conclusively
704 established that there are indeed variations in the robustness (as denoted by ABD/DIA
705 coupling) and duration of ABD responses, with the more rostral locations (+0.6 mm and
706 +0.8 mm from VIIc) yielding the most potent responses in this regard. Importantly, the
707 group with injection sites at +0.6 mm rostral to VIIc exhibited the swiftest response
708 onset, suggesting the closest proximity to, or the largest density of, the cells responsible
709 for ABD recruitment following bicuculline injection. Given that the total number of cFos+
710 cells did not vary across injection sites, it is conceivable to infer that the rostral pFL is in
711 the closest proximity to the cells responsible for the generation of active expiration.

712 *Bicuculline injection elicited stronger respiratory effects at rostral locations in pFL*

713 Bicuculline injections induced significant alterations in a number of respiratory
714 parameters, reminiscent of previous studies exploring the effects of
715 bicuculline/strychnine injections in the ventral medulla (de Britto & Moraes, 2017;
716 Pagliardini et al., 2011; Silva et al., 2019). We observed a drop in respiratory frequency
717 concomitant with the emergence of ABD recruitment in the caudal locations (-0.2 mm,
718 +0.1 mm), similar to what was observed in those locations through pharmacological
719 activation of pFL (Boutin et al., 2017; Pagliardini et al., 2011). However, in the most
720 rostral locations in our study (+0.4 mm, +0.6 mm, +0.8 mm), the respiratory frequency
721 remained unchanged. This dichotomy in the frequency response despite the presence
722 of ABD recruitment in both cases may suggest that the slowing of the respiratory period
723 in the most caudal locations may be a consequence of disinhibition of the adjacent
724 Bötzinger complex. Additional evidence to support this view is that the nadir of
725 respiratory frequency was achieved at increasing periods of time as the injections were
726 located increasingly more rostrally, with the most caudal injection reaching the minimum
727 respiratory frequency at 2 min post-injection, while at the most rostral injection site, the
728 minimum respiratory frequency was observed at 6 min.

729 On the other hand, V_T increased by 16-29% in all the studied locations except -0.2 mm,
730 similar to what was observed previously with activation of pFL at locations ranging from
731 -0.2 mm to +0.4 mm (Boutin et al., 2017; Pagliardini et al., 2011). However, minute
732 ventilation increased significantly above baseline at the +0.6 mm location in our study,
733 whereas it decreased at the -0.2 mm location and remained unchanged in the rest of
734 the sites. These results are in agreement with previous observations, where V_E
735 remained unchanged at caudal locations after bicuculline injection (-0.2 mm to +0.4
736 mm) (Pagliardini et al., 2011). However, it is important to highlight the absence of
737 studies that have measured V_T and V_E after eliciting active expiration at more rostral
738 locations (+0.6 mm to +0.8 mm) (Silva et al., 2019). These results emphasize that the
739 rostro-caudal organization of pFL is not as simple as previously thought and particularly
740 highlights the importance of studying more rostral locations that have previously been
741 neglected.

742 *Injection of bicuculline decreased oxygen consumption at the rostral locations*

743 This research also explored the metabolic consequences of bicuculline-induced
744 respiratory changes. We observed a significant decrease in V_{O2} at the most rostral
745 locations (+0.6 mm, +0.8 mm), which were also the sites where we observed the largest
746 changes in V_T and V_E produced by the injection of bicuculline. It is important to note that
747 these changes in V_T and V_E were not due to physiological needs and, therefore, could
748 be considered a form of artificial hyperventilation that would cause a drop in arterial
749 pCO_2 (Daly Md Fau - Hazzledine & Hazzledine, 1963) and affect the gas exchange
750 processes in the blood and peripheral tissues to reduce V_{O2}. Alternatively, the
751 abdominal recruitment induced by bicuculline might not only increase V_T and V_E but
752 might also facilitate respiratory mechanics *in vivo* (Bosc, Resta, Walker, & Kanagy,
753 2010; Giordano, 2005; Haupt, Goodman Dm Fau - Sheldon, & Sheldon, 2012; Ninane,
754 Rypens F Fau - Yernault, Yernault Jc Fau - De Troyer, & De Troyer, 1992; Ninane,
755 Yernault Jc Fau - de Troyer, & de Troyer, 1993), reducing the work of breathing and,
756 subsequently, causing a significant reduction in O_2 consumption. This remains to be
757 determined, however.

758 *Rostral pFL bicuculline injections induces more prominent changes to all phases of the*
759 *respiratory cycle*

760 Here we introduced a novel, area-under-the-curve (AUC) analysis algorithm, aimed at
761 dissecting the respiratory changes evoked within each phase of the respiratory cycle
762 (late-E, Inspiration, post-I) as a result of the locale of injections and relative to baseline
763 conditions for each of the airflow, DIA and ABD signals. This method revealed that the
764 two most rostral injection sites elicited the most robust activation of ABD activity and
765 induced the most significant alterations in expiratory airflow during both the late-E and
766 post-I phases. Similarly, during the inspiratory phase, rostral injections generated the
767 most pronounced changes in inspiratory airflow and DIA activity - particularly when
768 positioned +0.6mm from the VIIc. These findings align with the observed increases in
769 tidal volume depicted in Figure 4 H-I at those specific locations. Moreover, in the post-I
770 phase, we also observed the most prominent negative airflow deflections at the most

771 rostral injection sites, corresponding to concurrent ABD activation during that same
772 timeframe.

773 By applying this novel analytical approach, which, to the best of our knowledge, has not
774 been previously employed in research evaluating ABD responses triggered by pFL
775 activation (Boutin et al., 2017; de Britto & Moraes, 2017; Huckstepp et al., 2015; Korsak
776 et al., 2018; Magalhães et al., 2021; Pagliardini et al., 2011; Silva et al., 2019; Zoccal et
777 al., 2018), we were able to reveal disparities in the AUC of ABD and airflow signals.
778 These disparities, which went undetected with the analyses shown in Figure 4B to E,
779 were particularly evident during the late-E and post-I periods. Furthermore, the division
780 of the response into three distinct respiratory phases enabled a more precise
781 assessment of how targeted stimulation affects a particular phase of the respiratory
782 cycle, which could be used in future research to provide valuable insights into the
783 underlying neural mechanisms of respiratory control.

784 *Bicuculline responses following injections along the rostro-caudal axis of the ventral*
785 *medulla can be differentiated by the time course and total extent of respiratory*
786 *activation during late-E, inspiration and post-I phases.*

787 Our results certainly indicate that bicuculline injections at various pFL locations induce a
788 complex set of interactions between DIA and ABD muscle activation, as well as changes
789 in airflow across the inspiratory and expiratory phases of respiration. Our final goal was
790 to develop an algorithm which could accurately represent the complete “framework” of
791 respiratory activation across each recorded signal with respect to each these phases.
792 To this end, we introduced another novel analysis method that tracked the multivariate
793 variations occurring throughout the respiratory cycle. We were able to visualize and
794 highlight a number of features of the respiratory cycle including late-E “tails”, inspiratory
795 “bulbs” and post-I “feet” that allowed us to characterize alterations that are specifically
796 relevant to active expiration. Given that this analysis is designed to maintain a
797 consistent representation across conditions within experiments, these features can be
798 catalogued into a “framework” of the breathing cycle during both baseline and post-
799 injection conditions. Thus, this method is both sensitive to subtle changes in the

activations of each component signal, but also more importantly, it is highly robust to the variability inherent in the acquisition of respiratory physiological measurements *in vivo*.

By quantifying the respiratory cycle in terms of 3D measures of distance we were able to differentiate between the rostral and caudally evoked responses, as well as differences between the two most rostral locations which were previously undetected in the standard analyses as presented in Figure 4 B-E. Particularly, our findings were consistent with the other analyses applied here with regards to the significantly larger extent of respiratory loop distortions in the two most rostral positions in comparison to the more caudal injections. Furthermore, it was observed that injections in the +0.8mm group produced the highest amplitude changes to the late-E “tails” which also persisted for a more extended duration. Injections at this location also produced significant post-I “feet” for a longer period of time. Conversely, the most prominent inspiratory “bulbs” were observed in the +0.6 mm group, aligning with the most substantial changes in V_T observed in Figure 4 H-I.

Collectively, these results imply that while the combined effects of bicuculline injection on the respiratory cycle were most pronounced at the two most rostral positions, there were slight variations in the effects exhibited during each respiratory phase at this level of the ventral medulla. These nuanced effects may suggest differences in the functional characteristics, phenotypes and projections of cell populations at these specific coordinates. It is worth noting that the pFL neurons responsible for active expiration are typically quiescent in adults at rest (de Britto & Moraes, 2017; Magalhães et al., 2021; Pagliardini et al., 2011), making their phenotypic and functional characterization challenging. Recent research has indicated that the pFL cells exhibiting late-E firing during hypercapnia-induced active expiration are characterized as glutamatergic, phox2b-negative and NMB-negative, and possess TASK, GPR4, hyperpolarization-activated, cyclic nucleotide-gated, T-type Calcium, and twik related K+ leak channels, while they lack sodium persistent current channels (Magalhães et al., 2021). However, these observations were made in neurons situated closer to the tip of the facial nucleus in juvenile rats. It will be important to investigate now whether phenotypic and electrical properties of neurons at more rostral positions share the same identity.

830 *pFL or RTN?*

831 An ongoing debate centers on whether the neurons responsible for the generation of
832 ABD recruitment are an independent oscillator composed of PHOX2B-, late-E firing
833 neurons (pFL) (de Britto & Moraes, 2017; Magalhães et al., 2021; Pagliardini et al.,
834 2011; Pisanski & Pagliardini, 2019) or part of the PHOX2B+/NMB+ chemosensitive
835 neurons of the RTN/ventral paraFacial region (Abbott, Stornetta, Coates, & Guyenet,
836 2011; George, Ruth, Daniel, Stephen, & Patrice, 2020; Marina et al., 2010). While there
837 is evidence that specific stimulation of PHOX2B+/NMB+ neurons causes ABD activity
838 and active expiration (Abbott et al., 2011; George et al., 2020), these studies have not
839 shown recordings from late-E PHOX2B/NMB+ neurons in their investigations. However,
840 there is concrete evidence of the existence of PHOX2B-negative late-E firing neurons
841 that are activated in response to bicuculline injections in the ventral medulla (de Britto &
842 Moraes, 2017; Magalhães et al., 2021; Pagliardini et al., 2011) while PHOX2B/NMB+
843 chemosensitive neurons may send tonic excitatory drive to the expiratory oscillator
844 when activated. Because our anatomical results show very little PHOX2B/cFos+
845 staining at injections sites rostral to +0.1 mm, is fair to conclude that the ABD activity
846 generated at that level is likely not the direct result of RTN activation or driven by
847 PHOX2B+ neurons.

848 *Conclusion*

849 The results of this study highlight the functional diversity of the lateral parafacial region
850 and emphasize the strong role of the most rostral locations in generating active
851 expiration. The use of our novel multi dimensional map to assess physiological
852 responses highlighted the functional nuances in respiratory responses to bicuculline
853 along the pFL rostrocaudal axis, and advanced our understanding of the parafacial
854 region.

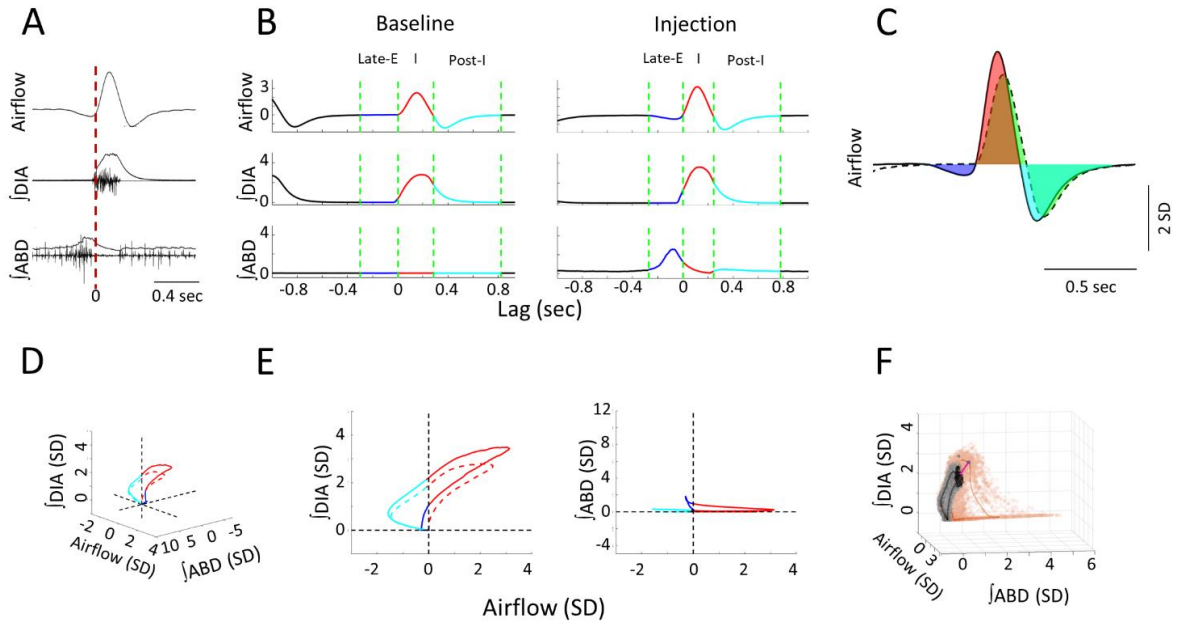

Figure 1

Measures used in quantifying respiratory responses to bicuculline injections. A: The time course of raw, and integrated EMG signals relative to recorded airflow during a sample breath. Vertical red line indicates the onset of inspiration as defined by positive airflow. B: Respiratory phases within a mean-cycle computed during baseline and post-injection for each recorded signal. Green lines mark the boundaries of each phase of the respiratory cycle, including the late-E (Blue), inspiratory (Red), and post-I (cyan) phases. C: Sample calculation of normalized area-under the-curve. Area under the baseline mean-cycle (dashed line, area in green) in each phase is subtracted from the corresponding colored area under the response mean-cycle (solid line, late-E: Blue, inspiration: Red, post-I: Cyan) to give a measure of how inspiratory airflow has changed relative to baseline. D: 3D representation of a representative baseline (dashed line) and response (solid line) mean-cycle. Each timepoint is a dot in 3D space defined by its airflow, ∫DIA EMG, and ∫ABD EMG measurements. Colors indicate respiratory sub-periods as in B. Dashed lines indicate the origin for each measure. E: 2D projection of the mean-cycle in D. As per the colors in B, points on the left-hand side indicate

expiration, points on the right-hand side indicate inspiration. F: Sample calculation of Euclidean and Mahalanobis distance measures for representative mean-cycles during the baseline (gray) and response (orange). PinkGreen line indicates the Euclidean distance between the response and baseline at a single timepoint. Black indicates the distribution of baseline values at the same timepoint used to calculate the Mahalanobis distance. Mean-cycles have been rotated relative to D to expose these distances to the viewer.

879

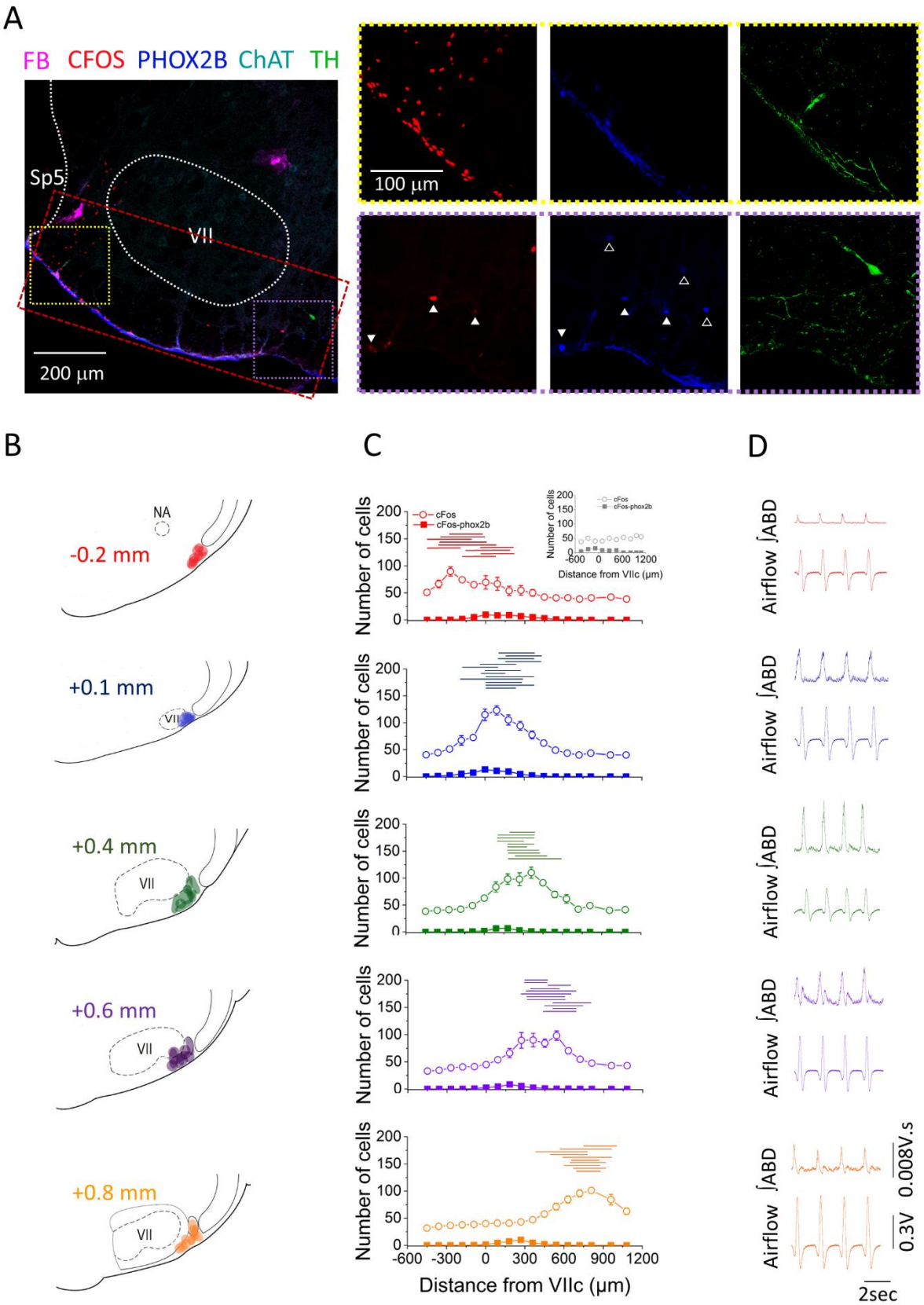
A
FB CFOS PHOX2B ChAT TH
Sp5
VII
200 µm
100 µm
B
NA
-0.2 mm
+0.1 mm
VII
+0.4 mm
+0.6 mm
+0.8 mm
C
cFos
cFos-phox2b
Number of cells
Distance from VIIc (µm)
D
Airflow
∫ABD
0.008V.s
0.3V
2sec

880 Figure 2

881 *Location of bicuculline injections along the rostrocaudal axis of the ventral medulla*. A:
882 Representative confocal microscope images of immunohistochemistry performed at the
883 injection sites. Red: cFos, Cyan: ChAT, Blue: PHOX2B, Green: TH, Magenta:
884 fluorobeads. Red rectangle is a representative example of the area used for cell
885 counting. Yellow and Purple squares are the areas represented on the right panel of A,
886 notice the abundance of CFOS+ cells on the lateral area near the injection site (yellow
887 square) compared to the fewer CFOS+ cells in the medial area (purple square). Closed
888 white triangles are pointing out examples of CFOS-PHOXB+ cells, whereas open white
889 triangles are pointing out examples of PHOX2B+ cells that were CFOS-negative.
890 Magnification is the same for all images in the right panels of A. B: Schematic
891 representation of the core of the injection sites and the group attribution, according to
892 proximity of injection sites among experimental rats (-0.2 mm, n=5; +0.1 mm n=7; +0.4
893 mm, n=5; +0.6 mm, n=6; +0.8 mm, n=5). C: Cell counting colored coded according to
894 the groups defined in B (CTRL, n=7; -0.2 mm, n=5; +0.1 mm n=7; +0.4 mm, n=5; +0.6
895 mm, n=6; +0.8 mm, n=5). Data points represents the Mean ± SEM of cells counted per
896 hemisection at rostrocaudal locations ranging from -0.5 to +1.0 mm from VIIc. Open
897 circles: CFOS+ cells; Closed squares: CFOS/PHOX2B+ cells. Inset in group -0.2 mm is
898 the cell count obtained for the CTRL group. Horizontal lines above the cell count graphs
899 represent the rostrocaudal extension in which fluorobeads were observed for each
900 injection site. D: Representative examples of ∫ABD EMG and Raw Airflow traces
901 obtained after injection of bicuculline (color coded based on the groups defined in B).

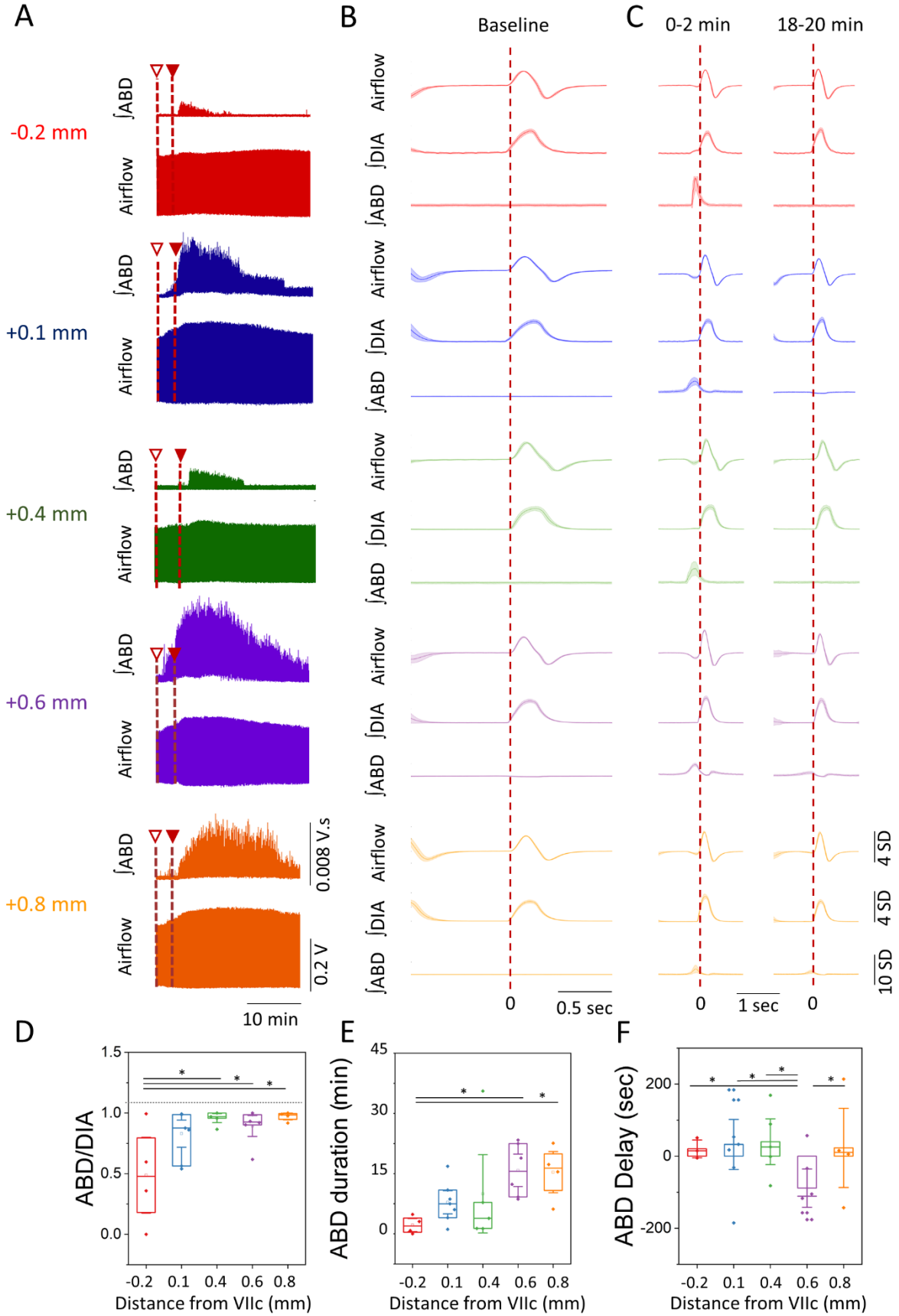
A
-0.2 mm
+0.1 mm
+0.4 mm
+0.6 mm
+0.8 mm
∫ABD
Airflow
0.008 V.s
0.2 V
10 min
B
Baseline
C
0-2 min
18-20 min
∫DIA
0
0.5 sec
1 sec
4 SD
10 SD
D
ABD/DIA
E
ABD duration (min)
F
ABD Delay (sec)
Distance from VIIc (mm)
-0.2
0.1
0.4
0.6
0.8

Figure 3

Temporal Characteristics of the ABD response elicited after bicuculline injection. A: Representative examples of raw traces of the Airflow and ∫ABD EMG signals for the entire duration of the response obtained at each injection site following the first (open triangle) and second injection (closed triangle) of bicuculline (examples are colored coded based on the groups obtained in Figure 2 B). B-C: Representative mean-cycles for the Airflow, ∫DIA EMG, and ∫ABD EMG during baseline (B) and during the first two min and the last two min of the response (C) (traces are color coded based on the groups defined in Figure 2 B). Shaded areas indicate standard deviation of each signal. D: Coupling of the ∫ABD EMG and ∫DIA EMG following the injection of bicuculline at different rostrocaudal locations. E: Duration of the ABD response elicited. F: Delay in the onset of the ABD response following the second injection of bicuculline. Sample size for plots on D-F are as follow: -0.2 mm, n=5; +0.1 mm n=7; +0.4 mm, n=5; +0.6 mm, n=6; +0.8 mm, n=5. Boxplots represent the median, interquartile range, as well as the minimum and maximum values. Significance levels were obtained through a One-Way ANOVA followed by a Tukey Test, $p<0.005$.

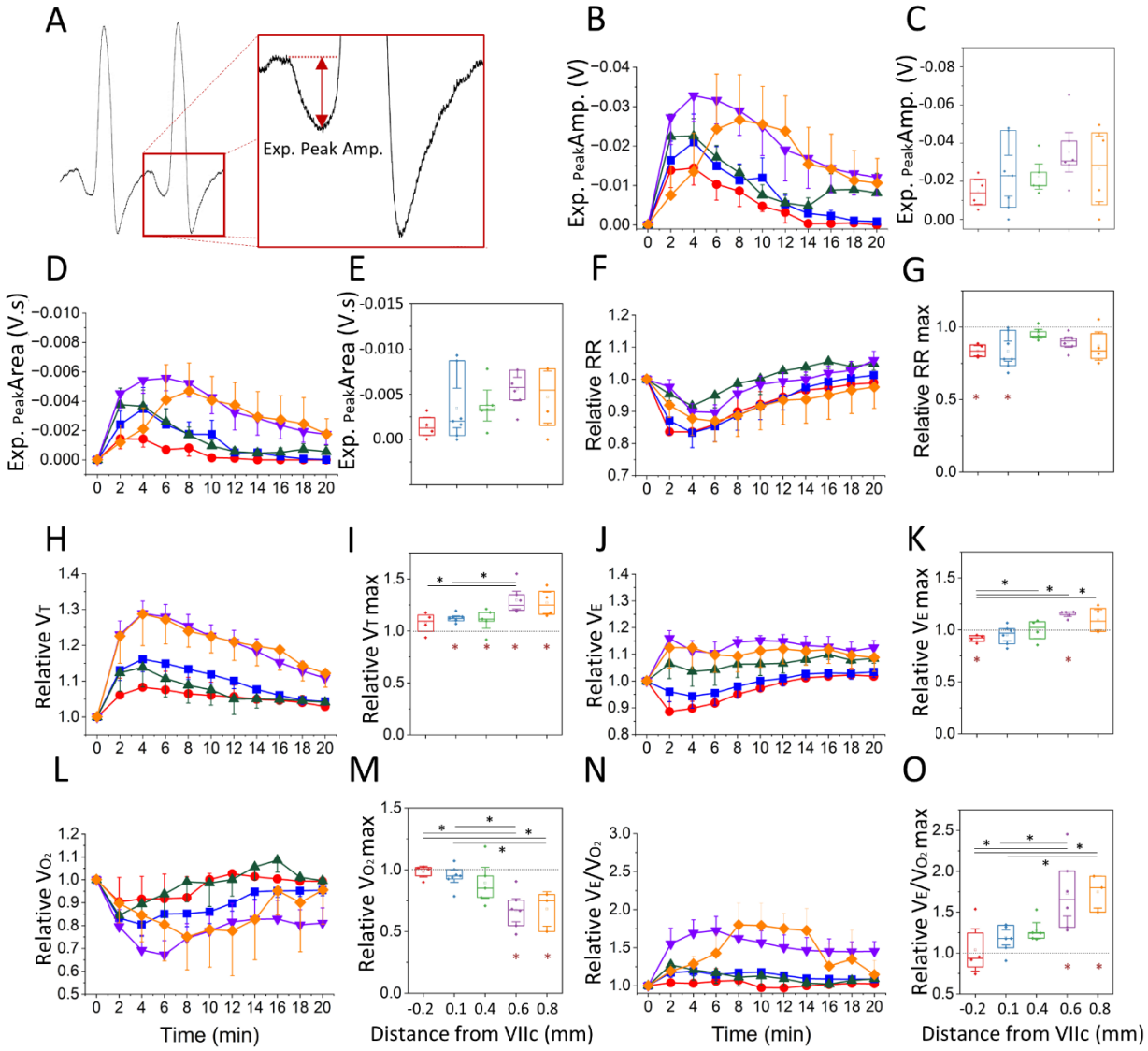

Figure 4:

Respiratory Changes elicited following bicuculline injection: A: Airflow trace depicting the late expiratory (Late-E) inward airflow inflection induced during ABD recruitment, as well as the measure of Expiratory Peak Amplitude used in B. B,D: Expiratory Peak Amplitude (B) and Area (D), throughout the duration of the post-injection period for each group (color coded based in Figure 2 B). Values represent the Mean ± SEM at each time bin. C,E: Maximum Expiratory Peak Amplitude (C) and Area (E) obtained at each injection site. F,H,J,L,N: Relative change in respiratory rate (F), Tidal Volume (H), Minute Ventilation (J), Oxygen Consumption (L) and V_E/V_{O2} (N) with respect to baseline

throughout the duration of the post-injection period for each group (color coded based on Figure 2 B). Values represent the Mean ± SEM at each time bin. G,I,K,M,O: Maximum relative change in respiratory rate (G), Tidal Volume (I), Minute Ventilation (K), Oxygen Consumption (M) and V_E/V_{O2} (O) observed at each injection site. Sample size for plots on B-O are as follow: -0.2 mm, n=5; +0.1 mm n=7; +0.4 mm, n=5; +0.6 mm, n=6; +0.8 mm, n=5. Boxplots represent the median, interquartile range, as well as the minimum and maximum values. Significance levels were obtained through a One-Way Repeated Measures ANOVA followed by a Bonferroni Test, $p<0.005$ (black asterisks represent significant comparisons between injection sites, red asterisks represent significant comparisons relative to baseline).

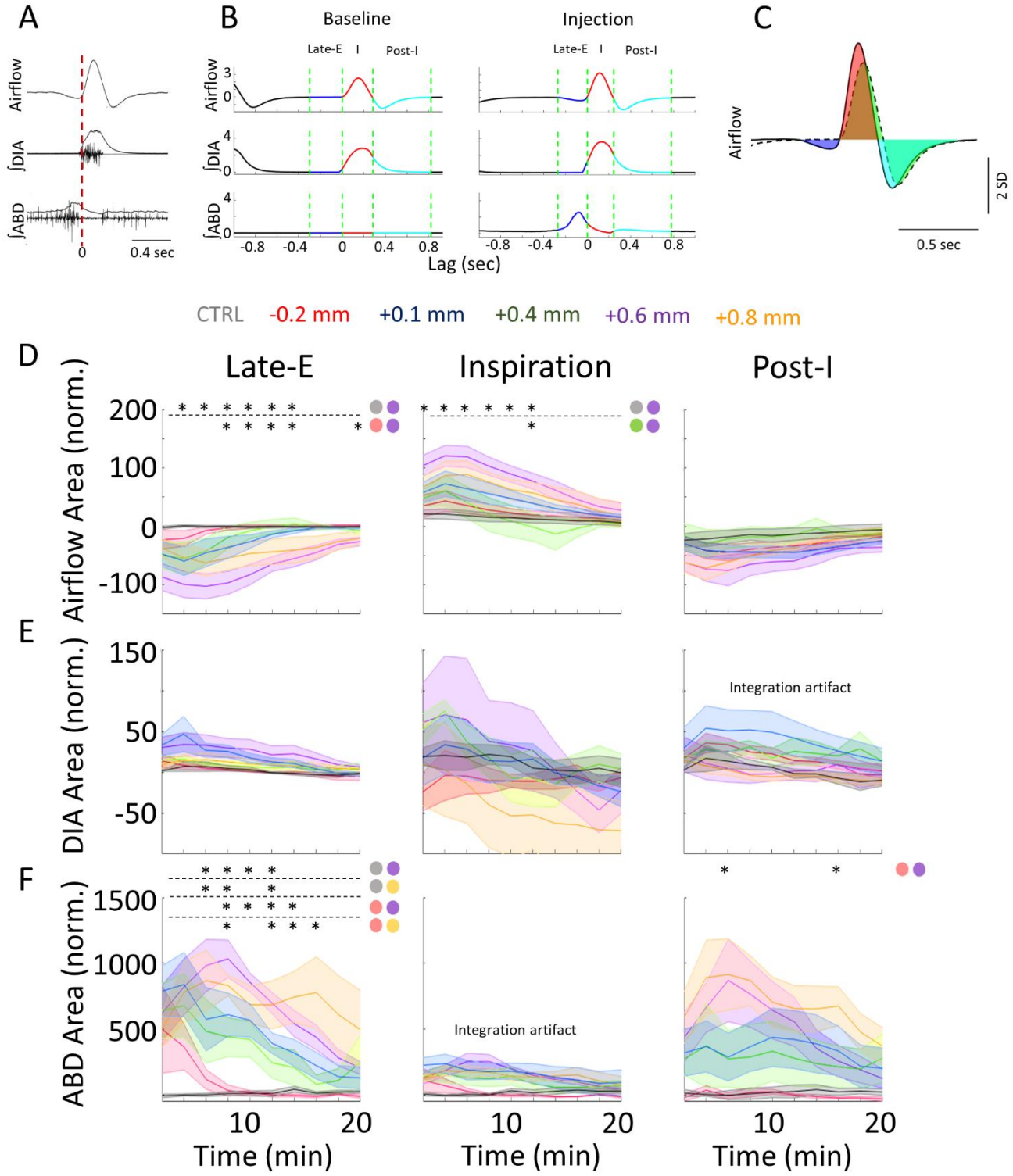
A
Airflow
∫DIA
∫ABD
0
0.4 sec
B
Baseline
Injection
Late-E
I
Post-I
Lag (sec)
C
Airflow
2 SD
0.5 sec
CTRL
-0.2 mm
+0.1 mm
+0.4 mm
+0.6 mm
+0.8 mm
D
Late-E
Inspiration
Post-I
Airflow Area (norm.)
E
DIA Area (norm.)
Integration artifact
F
ABD Area (norm.)
Integration artifact
Time (min)

Figure 5:

Rostral injections elicit more prominent changes to respiration in each signal and sub-period. A: Raw and integrated EMG activity relative to the onset of inspiration (vertical line). B: Representative mean-cycles during the baseline and post-injection, defining the late-E (Blue), inspiratory (Red), and post-I (Cyan) periods. C: Sample calculation of normalized area during each phase. D-F: Normalized response area across post-injection time for the Airflow (D), ∫DIA EMG (E), and ∫ABD EMG (F) signals following bicuculline injections into various coordinates along the rostral-caudal axis (colors as per label above figure). Sample size for plots on D-F are as follow: CTRL, n=7; -0.2 mm, n=5; +0.1 mm n=7; +0.4 mm, n=5; +0.6 mm, n=6; +0.8 mm, n=5. Stars indicate a significant difference (p <0.05) between the responses elicited by different injection locations (color-coded based on the groups defined in Figure 2 B) as assessed via Kruskal-Wallis test. Colored circles indicate the comparisons which were significant as per Dunn's post-hoc test with Sidak's correction. Shaded areas indicate mean + SEM.

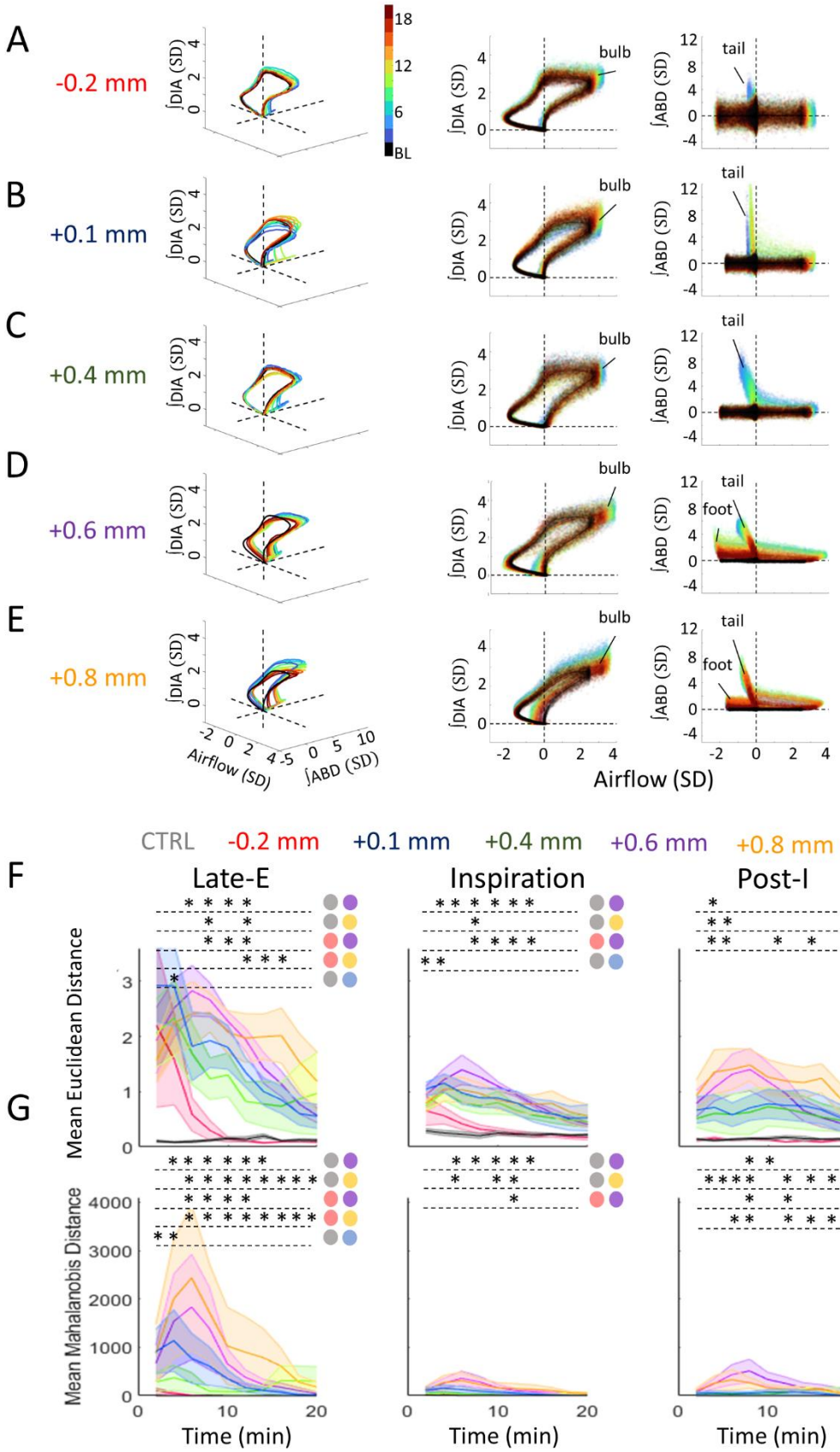
A
-0.2 mm
B
+0.1 mm
C
+0.4 mm
D
+0.6 mm
E
+0.8 mm
∫DIA (SD)
∫ABD (SD)
Airflow (SD)
bulb
tail
foot
18
12
6
BL
CTRL
-0.2 mm
+0.1 mm
+0.4 mm
+0.6 mm
+0.8 mm
F
Late-E
Inspiration
Post-I
G
Mean Euclidean Distance
Mean Mahalanobis Distance
Time (min)

Figure 6:

Deformations in multivariate respiratory trajectories differentiate the responses of various rostrocaudal coordinates following bicuculline injections. A-E: Representative respiratory trajectories from each injection location. Each row shows the 3D trajectories (solid lines) of the mean-cycle computed for baseline (black) and response time bins (blue to red), based on the color legend in the 3D panel of A. 2D projections of these trajectories onto the airflow-∫DIA EMG (middle), and airflow-∫ABD EMG planes (right) follow on the right of each 3D figure. Clouds of coloured points surrounding each trajectory indicate values from individual cycles of the corresponding time bin. Dashed lines indicate the origin of each axis. F: Mean Euclidean distance across response time bins comparing each injection location for the late-E, inspiratory, and post-I phases. Colours as per Figure 5, noted above the figure. Shaded areas indicate Mean +/- SEM. Stars indicate significance ($p < 0.05$) for a given time bin between injection locations or control injections as determined by Kruskal-Wallis test. Colored circles indicate which groups were significantly different as per Dunn post-hoc testing with Sidak's correction. G: Mean Mahalanobis distance across the post-injection response for each injection location and respiratory phase. Colors as in F. Sample size for plots on F-G are as follow: CTRL, n=7; -0.2 mm, n=5; +0.1 mm n=7; +0.4 mm, n=5; +0.6 mm, n=6; +0.8 mm, n=5. Shaded areas indicate Mean +/- SEM. Stars indicate significance at the $p = 0.05$ level between injection locations for a given time bin as determined by Kruskal-Wallis test. Colored circles indicate which groups were significantly different as per Dunn post-hoc with Sidak's correction.

Supplementary File 1:

Rotating 3D respiratory trajectories highlight the features of breathing in baseline and response conditions. Trajectories from the sample recordings in Figure 6A (-0.2mm) across baseline and response time bins (colored as per color bar on right. Each dot represents a time point from a given time bin. A subsample of ~11000 timepoints from each time bin have been randomly selected and are rotated about the DIA axis to highlight the architecture of respiratory trajectories. Dashed lines indicate the origin of each axis. Axis values expressed in units of standard deviation (SD) as per methods description.

Supplementary File 2:

Rotating 3D respiratory trajectories highlight the features of breathing in baseline and response conditions. Trajectories from the sample recordings in Figure 6B (+0.1mm) across baseline and response time bins (colored as per color bar on right. Each dot represents a time point from a given time bin. A subsample of ~11000 timepoints from each time bin have been randomly selected and are rotated about the DIA axis to highlight the architecture of respiratory trajectories. Dashed lines indicate the origin of each axis. Axis values expressed in units of standard deviation (SD) as per methods description.

Supplementary File 3:

Rotating 3D respiratory trajectories highlight the features of breathing in baseline and response conditions. Trajectories from the sample recordings in Figure 6AC (+0.4mm) across baseline and response time bins (colored as per color bar on right. Each dot represents a time point from a given time bin. A subsample of ~11000 timepoints from each time bin have been randomly selected and are rotated about the DIA axis to highlight the architecture of respiratory trajectories. Dashed lines indicate the origin of each axis. Axis values expressed in units of standard deviation (SD) as per methods description.

Supplementary File 4:

Rotating 3D respiratory trajectories highlight the features of breathing in baseline and response conditions. Trajectories from the sample recordings in Figure 6D (+0.6mm) across baseline and response time bins (colored as per color bar on right. Each dot represents a time point from a given time bin. A subsample of ~11000 timepoints from each time bin have been randomly selected and are rotated about the DIA axis to highlight the architecture of respiratory trajectories. Dashed lines indicate the origin of each axis. Axis values expressed in units of standard deviation (SD) as per methods description.

Supplementary File 5:

Rotating 3D respiratory trajectories highlight the features of breathing in baseline and response conditions. Trajectories from the sample recordings in Figure 6E (+0.8mm) across baseline and response time bins (colored as per color bar on right. Each dot represents a time point from a given time bin. A subsample of ~11000 timepoints from each time bin have been randomly selected and are rotated about the DIA axis to highlight the architecture of respiratory trajectories. Dashed lines indicate the origin of each axis. Axis values expressed in units of standard deviation (SD) as per methods description.

References

Abbott, S. B. G., Stornetta, R. L., Coates, M. B., & Guyenet, P. G. (2011). Phox2b-expressing neurons of the parafacial region regulate breathing rate, inspiration, and expiration in conscious rats. *Journal of Neuroscience, 31*(45), 16410-16422. doi:10.1523/JNEUROSCI.3280-11.2011

Biancardi, V., Yang, X., Ding, X., Passi, D., Funk, G. D., & Pagliardini, S. (2023). Cholinergic projections to the preBötzinger complex. *Journal of Comparative Neurology, 531*(13), 1317-1332. doi:https://doi.org/10.1002/cne.25497

Bosc, L. V. G., Resta, T., Walker, B., & Kanagy, N. L. (2010). Mechanisms of intermittent hypoxia induced hypertension. *Journal of Cellular and Molecular Medicine, 14*(1-2), 3-17. doi:https://doi.org/10.1111/j.1582-4934.2009.00929.x

Boutin, R. C. T., Alsahafi, Z., & Pagliardini, S. (2017). Cholinergic modulation of the parafacial respiratory group. *Journal of Physiology, 595*(4), 1377-1392. doi:10.1113/JP273012

Daly Md Fau - Hazzledine, J. L., & Hazzledine, J. L. (1963). THE EFFECTS OF ARTIFICIALLY INDUCED HYPERVENTILATION ON THE PRIMARY CARDIAC REFLEX RESPONSE TO STIMULATION OF THE CAROTID BODIES IN THE DOG. (0022-3751 (Print)).

de Britto, A. A., Magalhães, K. S., da Silva, M. P., Paton, J. F. R., & Moraes, D. J. A. (2020). Active expiratory oscillator regulates nasofacial and oral motor activities in rats. *Experimental Physiology, 105*(2), 379-392. doi:https://doi.org/10.1113/EP088046

de Britto, A. A., & Moraes, D. J. A. (2017). Non-chemosensitive parafacial neurons simultaneously regulate active expiration and airway patency under hypercapnia in rats. *Journal of Physiology, 595*(6), 2043-2064. doi:10.1113/JP273335

Del Negro, C. A., Funk, G. D., & Feldman, J. L. (2018). Breathing matters. *Nature Reviews Neuroscience, 19*(6), 351-367. doi:10.1038/s41583-018-0003-6

George, M. P. R. S., Ruth, L. S., Daniel, S. S., Stephen, B. G. A., & Patrice, G. G. (2020). Differential Contribution of the Retrotrapezoid Nucleus and C1 Neurons to Active Expiration and Arousal in Rats. *The Journal of Neuroscience, 40*(45), 8683. doi:10.1523/JNEUROSCI.1006-20.2020

Giordano, F. J. (2005). Oxygen, oxidative stress, hypoxia, and heart failure. *The Journal of Clinical Investigation, 115*(3), 500-508. doi:10.1172/JCI24408

Gray, P. A., Janczewski, W. A., Mellen, N., McCrimmon, D. R., & Feldman, J. L. (2001). Normal breathing requires preBötzinger complex neurokinin-1 receptor-expressing neurons. *Nature Neuroscience, 4*(9), 927-930. doi:10.1038/nn0901-927

Haupt, M. E., Goodman Dm Fau - Sheldon, S. H., & Sheldon, S. H. (2012). Sleep related expiratory obstructive apnea in children. (1550-9397 (Electronic)).

Hayes, J. A., Kottick, A., Picardo, M. C. D., Halleran, A. D., Smith, R. D., Smith, G. D., . . . Del Negro, C. A. (2017). Transcriptome of neonatal preBötzinger complex neurones in Dbx1 reporter mice. *Scientific Reports, 7*(1), 8669. doi:10.1038/s41598-017-09418-4

Huckstepp, R. T. R., Cardoza, K. P., Henderson, L. E., & Feldman, J. L. (2015). Role of parafacial nuclei in control of breathing in adult rats. *Journal of Neuroscience, 35*(3), 1052-1067. doi:10.1523/JNEUROSCI.2953-14.2015

Janczewski, W. A., Onimaru, H., Homma, I., & Feldman, J. L. (2002). Opioid-resistant respiratory pathway from the preinspiratory neurones to abdominal muscles: in vivo and in vitro study in the newborn rat. *The Journal of Physiology, 545*(3), 1017-1026. doi:https://doi.org/10.1113/jphysiol.2002.023408

Korsak, A., Sheikhbahaei, S., Machhada, A., Gourine, A. V., & Huckstepp, R. T. R. (2018). The Role Of Parafacial Neurons In The Control Of Breathing During Exercise. *Scientific Reports, 8*(1), 1-12. doi:10.1038/s41598-017-17412-z

Leirão, I. P., Silva, C. A., Gargaglioni, L. H., & da Silva, G. S. F. (2018). Hypercapnia-induced active expiration increases in sleep and enhances ventilation in unanaesthetized rats. *Journal of Physiology, 596*(15), 3271-3283. doi:10.1113/JP274726

Magalhães, K. S., da Silva, M. P., Mecawi, A. S., Paton, J. F. R., Machado, B. H., & Moraes, D. J. A. (2021). Intrinsic and synaptic mechanisms controlling the expiratory activity of excitatory lateral parafacial neurones of rats. *The Journal of Physiology, 599*(21), 4925-4948. doi:https://doi.org/10.1113/JP281545

Marina, N., Abdala, A. P., Trapp, S., Li, A., Nattie, E. E., Hewinson, J., . . . Gourine, A. V. (2010). Essential role of Phox2b-expressing ventrolateral brainstem neurons in the chemosensory control of inspiration and expiration. *Journal of Neuroscience, 30*(37), 12466-12473. doi:10.1523/JNEUROSCI.3141-10.2010

Ninane, V., Rypens F Fau - Yernault, J. C., Yernault Jc Fau - De Troyer, A., & De Troyer, A. (1992). Abdominal muscle use during breathing in patients with chronic airflow obstruction. (0003-0805 (Print)).

Ninane, V., Yernault Jc Fau - de Troyer, A., & de Troyer, A. (1993). Intrinsic PEEP in patients with chronic obstructive pulmonary disease. Role of expiratory muscles. (0003-0805 (Print)).

Onimaru, H., & Homma, I. (2003). A novel functional neuron group for respiratory rhythm generation in the ventral medulla. *Journal of Neuroscience, 23*(4), 1478-1486.

Onimaru, H., Kumagawa, Y., & Homma, I. (2006). Respiration-Related Rhythmic Activity in the Rostral Medulla of Newborn Rats. *Journal of Neurophysiology, 96*(1), 55-61. doi:10.1152/jn.01175.2005

Pagliardini, S., Janczewski, W. A., Tan, W., Dickson, C. T., Deisseroth, K., & Feldman, J. L. (2011). Active expiration induced by excitation of ventral medulla in adult anesthetized rats. *Journal of Neuroscience, 31*(8), 2895-2905. doi:10.1523/JNEUROSCI.5338-10.2011

Pisanski, Ding, X., Koch, N. A., & Pagliardini, S. (2019). Chemogenetic modulation of the parafacial respiratory group influences the recruitment of abdominal activity during REM sleep. *Sleep*. doi:10.1093/sleep/zsz283

Pisanski, & Pagliardini, S. (2019). The parafacial respiratory group and the control of active expiration. *Respiratory Physiology and Neurobiology, 265*. doi:10.1016/j.resp.2018.06.010

Silva, J. N., Oliveira, L. M., Souza, F. C., Moreira, T. S., & Takakura, A. C. (2019). Distinct pathways to the parafacial respiratory group to trigger active expiration in adult rats. *American journal of physiology. Lung cellular and molecular physiology, 317*(3). doi:10.1152/ajplung.00467.2018

Smith, J. C., Ellenberger, H. H., Ballanyi, K., Richter, D. W., & Feldman, J. L. (1991). Pre-Bötzinger complex: A brainstem region that may generate respiratory rhythm in mammals. *Science, 254*(5032), 726-729. doi:10.1126/science.1683005

Tan, W., Janczewski, W. A., Yang, P., Shao, X. M., Callaway, E. M., & Feldman, J. L. (2008). Silencing preBötzinger Complex somatostatin-expressing neurons induces persistent apnea in awake rat. *Nature Neuroscience, 11*(5), 538-540. doi:10.1038/nn.2104

Wang, X., Hayes, J. A., Revill, A. L., Song, H., Kottick, A., Vann, N. C., . . . Del Negro, C. A. (2014). Laser ablation of Dbx1 neurons in the pre-Bötzinger complex stops inspiratory rhythm and impairs output in neonatal mice. *eLife, 3*(Xii), e03427-e03427. doi:10.7554/eLife.03427

Yackle, K., Schwarz, L. A., Kam, K., Sorokin, J. M., Huguenard, J. R., Feldman, J. L., . . . Krasnow, M. A. (2017). Breathing control center neurons that promote arousal in mice. *Science, 355*(6332), 1411-1415. doi:10.1126/science.aai7984

Yang, C. F., & Feldman, J. L. (2018). Efferent projections of excitatory and inhibitory preBötzinger Complex neurons. *Journal of Comparative Neurology, 526*(8), 1389-1402. doi:https://doi.org/10.1002/cne.24415

Yang, C. F., Kim, E. J., Callaway, E. M., & Feldman, J. L. (2020). Monosynaptic Projections to Excitatory and Inhibitory preBötzinger Complex Neurons. *Frontiers in Neuroanatomy, 14*. doi:10.3389/fnana.2020.00058

Zoccal, D. B., Silva, J. N., Barnett, W. H., Lemes, E. V., Falquetto, B., Colombari, E., . . . Takakura, A. C. (2018). Interaction between the retrotrapezoid nucleus and the parafacial respiratory group to regulate active expiration and sympathetic activity in rats. *American Journal of Physiology-Lung Cellular and Molecular Physiology, 315*(5), L891-L909. doi:10.1152/ajplung.00011.2018